(Ass.-Prof. Dr. Peter Rabl)

TU WIEN
TECHNISCHE
UNIVERSITÄT
WIEN
Vienna University of Technology

Diplomarbeit

$\mathcal{PT}$-symmetric systems in the quantum regime

Ausgeführt am

Atominstitut
der Technischen Universität Wien

unter der Anleitung von

Ass.-Prof. Dr. Peter Rabl

durch

Julian Huber
Matrikelnummer 1027246
Gfrornergasse 3/1/36
1060, Wien, Österreich
huberjulian@gmail.com

Wien am 18. Juli 2016

—————————————————
Julian Huber

Abstract

The phenomenon of $\mathcal{PT}$-symmetric breaking in classical systems with balanced loss and gain is associated with a sharp transition from a purely real to complex eigenvalue spectrum of the underlying dynamical matrix. Over the past years this phenomenon has been extensively studied, for example, using coupled optical modes, where however, the system is always in a large amplitude classical state. In this thesis we study for the first time the effect of $\mathcal{PT}$-symmetry breaking in the quantum regime where the effects of non-linearities and intrinsic quantum noise become important. In the first part we analyze the stationary states of two coupled harmonic oscillators with engineered loss and gain. By applying different numerical techniques to solve the corresponding master equation for this system we observe an unconventional transition from a high-noise symmetric state to a parity-broken lasing state with strongly reduced fluctuations. Moreover, we show that the transition point strongly depends on the quantumness of the system. In the second part we develop numerical techniques for the simulation of extended $\mathcal{PT}$-symmetric spin chains, which we use to demonstrate a crossover from a symmetric to a symmetry broken phase also for finite dimensional quantum systems.

Acknowledgements

Contents

II $\mathcal{PT}$-symmetric spin chains   55

6   Theoretical Framework   57

7   Numerical implementation   75

8   Results and Discussion   79

9   Conclusion   81

Bibliography   83

1 Introduction

One of the fundamental axioms in quantum mechanics is that the Hamiltonian operators corresponding to the total energy of a system are Hermitian $\mathcal{H} = \mathcal{H}^\dagger$. This conventional Hermiticity condition is sufficient to ensure that the Hamiltonian $\mathcal{H}$ has a real spectrum. However, Bender and Boettcher found a new class of non-Hermitian Hamiltonians with a purely real energy spectrum was found and attributed this fact to the underlying combined $\mathcal{PT}$ (parity and time reversal) symmetry [1]. This opened a whole new field of $\mathcal{PT}$-symmetric quantum theory, where the condition that the Hamiltonian is Hermitian is replaced by the weaker condition that it possesses invariance under space-time inversion ($\mathcal{PT}$-symmetry) [2]. Although these are purely mathematical considerations, there exist classical systems with balanced gain and loss which possess this symmetry. A $\mathcal{PT}$-symmetric system in the simplest configuration consists of two coupled harmonic oscillators, where one experiences gain while the other one experiences loss. This could be for example two coupled mechanical resonators [3, 4, 5].

The most interesting aspect of $\mathcal{PT}$-symmetry, is the breaking of the $\mathcal{PT}$-symmetry. At this breaking point the energy spectrum becomes complex and the eigenvectors no longer exhibit the underlying $\mathcal{PT}$-symmetry and the system undergoes a sharp transition from a purely oscillatory behavior to exponentially amplified and damped modes. This phenomenon has first been experimentally observed in optical waveguides [6] and is currently subject of intense experimental and theoretical research. One simple and elegant experiment is the coupling of two LRC circuits where one experiences gain while the other one experiences loss [7]. As well as that, experiments with typical classical objects such as a pair of coupled mechanical pendulums where carried out [8]. In all these experiments demonstrating $\mathcal{PT}$-symmetry breaking the two modes are in a highly classical state and the dynamics can be described by classical physics.

In this work we go beyond the classical picture and address for the first time an interesting and still open question: is there $\mathcal{PT}$-symmetry breaking in the quantum regime? We consider a minimal model consisting two coupled harmonic oscillators with engineered loss and gain. If the system is in the quantum regime the effects of non-linearities and intrinsic quantum noise become important. Compared to classical systems we have to introduce the open quantum system master equation formalism. A master equation describes in general a complicated problem and in this thesis we develop various numerical techniques to solve these problems.

The first part of this thesis is motivated by a recent work by K. V. Kepesidis et al.

[9], focusing on the steady states of $\mathcal{PT}$-symmetric phonon lasers in the presence of thermal noise, where also some results of my thesis were included.

The main goal of this thesis was to investigate observed $\mathcal{PT}$-symmetry breaking mechanism in the regime, where the system dynamics is affected by quantum noise only. Moreover we focus on the transition from the classical to the quantum regime and study the differences and the similarities.

In the second part we develop numerical techniques for the simulation of extended $\mathcal{PT}$-symmetric spin chains, which we use to study $\mathcal{PT}$-symmetry breaking in finite dimensional quantum systems.

2 $\mathcal{PT}$-symmetric systems

To motivate the following analysis by a concrete physical system, in this work we consider a setup of two coupled laser (conventional optical lasers or phonon lasers Figure 2.1) and spin chains (Figure 2.2). However, the main findings are more general and can be studied in other equivalent realizations.

2.1 Classical $\mathcal{PT}$-symmetric systems

A $\mathcal{PT}$-symmetric system in the simplest form consists of two coupled harmonic oscillators, where one experience gain while the other one experience loss. For such a gain-loss system the classical dynamics in rotating frame with respect to the oscillators frequency ω can be described by

$$\begin{pmatrix} \dot{\alpha} \\ \dot{\beta} \end{pmatrix} = \begin{pmatrix} \frac{\Gamma}{2} & -ig \\ -ig & -\frac{\Gamma}{2} \end{pmatrix} \begin{pmatrix} \alpha \\ \beta \end{pmatrix}, \tag{2.1}$$

where α and β are the classical amplitudes of the two systems, g the coupling strength between the two systems and Γ determines the strength of gain and loss. By comparing this equation with the Schrödinger equation $\dot{\psi} = -iH\psi$ for $\psi = (\alpha, \beta)^T$ one arrives at

$$H = \begin{pmatrix} i\frac{\Gamma}{2} & g \\ g & -i\frac{\Gamma}{2} \end{pmatrix}. \tag{2.2}$$

This non-Hermitian Hamiltonian is $\mathcal{PT}$-symmetric. By applying time-reversal $\mathcal{T}(i \rightarrow -i)$ and parity transformation $\mathcal{P}$ ($\alpha_1 \Leftrightarrow \alpha_2$), the equations do not change. The eigenvalues and (unnormalized) eigenvectors of the Hamiltonian are

$$\lambda_{1,2} = \pm\sqrt{g^2 - \frac{\Gamma^2}{4}}, \tag{2.3}$$

$$\psi_1 = \begin{pmatrix} e^{i\frac{\theta}{2}} \\ e^{-i\frac{\theta}{2}} \end{pmatrix}, \tag{2.4}$$

and

$$\psi_2 = \begin{pmatrix} ie^{-i\frac{\theta}{2}} \\ -ie^{i\frac{\theta}{2}} \end{pmatrix}, \tag{2.5}$$

respectively, where $\sin(\theta) = \Gamma/(2g)$ [10].

For $\frac{\Gamma}{2} < g$ both eigenvalues $\lambda_{1,2}$ are real. In this regime, the eigenvectors are eigenstates of the symmetry operator $\mathcal{PT}\psi_{1,2} = \psi_{1,2}$. For $\frac{\Gamma}{2} > g$, both eigenvalues become imaginary and correspond to a gain and a loss eigenmode. In this regime $\mathcal{PT}\psi_{1,2} \neq \psi_{1,2}$, i.e. the eigenvectors no longer have the same symmetry as the Hamiltonian. The $\mathcal{PT}$-symmetry breaks at $\frac{\Gamma}{2} = g$.

2.2 $\mathcal{PT}$-symmetric quantum systems

In this work we go beyond this usually considered classical systems and focus on open quantum systems. We emphasize that the joint dynamics of a quantum system and the surrounding bath is described by a unitary evolution operator generated by the Hermitian Hamiltonian of the total system. However, if we are only interested in the systems dynamics we can eliminate the bath degrees of freedom and describe the system in terms of a density operator ρ. As long as the coupling to the bath is weak the evolution of the density operator is given by a master equation. The master equation is trace preserving and therefore in contrast to the evolution under a non-Hermitian Hamiltonian, all probabilities are conserved.

For a simple $\mathcal{PT}$-symmetric system consisting of two coupled oscillators where one oscillator is heated and the other one cooled the master equation reads

$$\dot{\rho} = -\frac{i}{\hbar}[\mathcal{H}, \rho] + \frac{\Gamma}{2}\mathcal{D}[c_1^\dagger]\rho + \frac{\Gamma}{2}\mathcal{D}[c_2]\rho \tag{2.6}$$

with the Lindblad superoperator

$$\mathcal{D}[c]\rho \equiv 2c\rho c^\dagger - c^\dagger c\rho - \rho c^\dagger c. \tag{2.7}$$

The bosonic creation operator $c_1^\dagger$ in the argument of the Lindblad superoperator describes the gain of the first harmonic oscillator while the bosonic annihilation operator c_2 describes the loss of the second harmonic oscillator.

The Hamiltonian is given by

$$\mathcal{H} = \hbar\omega_c c_1^\dagger c_1 + \hbar\omega_c c_2^\dagger c_2 + \hbar g(c_1^\dagger c_2 + c_1 c_2^\dagger) \tag{2.8}$$

where ω_c is the oscillators frequency and g is the coupling strength between the two oscillators. By moving into a rotated frame with respect to ω_c and calculating the time evolution of the expectation values of c_1 and c_2 we get

$$\begin{pmatrix} \langle \dot{c}_1 \rangle \\ \langle \dot{c}_2 \rangle \end{pmatrix} = \begin{pmatrix} \frac{\Gamma}{2} & -ig \\ -ig & -\frac{\Gamma}{2} \end{pmatrix} \begin{pmatrix} \langle c_1 \rangle \\ \langle c_2 \rangle \end{pmatrix}. \tag{2.9}$$

We see that the creation operator $c_1^\dagger$ and annihilation operator c_2 in the argument of the Lindblad operator leads to linear gain and loss of the expectation values. By

comparing this equation with Equation 5.4 one arrives at the same phenomenological Hamiltonian as in the classical case (Equation 2.2).

Again there exists a symmetric regime, where the state will just oscillate in the complex plane and a broken regime, where the occupation of one oscillator will blow up and the occupation of the other one will be depleted. After infinite time one oscillator would have infinite energy which is of course very unphysical as every physical system e.g. an optical laser saturates at some point. To include this aspect into our model, we introduce a non-linearity in our toy model. We can write a general master equation

$$\dot{\rho} = -\frac{i}{\hbar}[\mathcal{H}, \rho] + \frac{\Gamma}{2}\mathcal{D}[c_g^\dagger]\rho + \frac{\Gamma}{2}\mathcal{D}[c_l]\rho \tag{2.10}$$

with the same Hamiltonian as before (Equation 5.3) but with effective ladder operator for gain

$$c_g^\dagger = c_1^\dagger\sqrt{f(n_1)} \tag{2.11}$$

and loss

$$c_l = \sqrt{f(n_2)}c_2 \tag{2.12}$$

where $f(n_i)$ is an arbitrary function only depending on $n_i = c_i^\dagger c_i$.

Although there are many possibilities for the non-linear function $f(n)$, we will focus on functions of the form

$$f(n) = \frac{1}{\left(1 + \frac{c^\dagger c}{n_0}\right)^\nu} \tag{2.13}$$

where n_0 is the saturation parameter. The saturation parameter n_0 determines the occupation in steady state and as a results denotes how quantum or classical a system is. A saturation $n_0 \approx 1$ can be referred to the quantum regime while a $n_0 \gg 1$ can be seen as the classical regime.
The form of the non-linear function is motivated by the semi-classical solution of the conventional optical laser equation ($\nu = 1$) [11] and the semi-classical equations for a phonon laser with NV-centers in diamond ($\nu = 2$) [12]. While an optical laser can be modeled by an inverted two-level system coupled to a cavity, a phonon laser can be realized by an optical-driven three-level defect (see Figure 2.1).

In the classical limit the gain and loss becomes

$$\Gamma(\alpha) = \frac{\Gamma}{\left(1 + \frac{|\alpha|^2}{n_0}\right)^\nu} \tag{2.14}$$

and for $\nu = 1$ this coincides with the classical laser equation and for $\nu = 2$ with the classical equations of a phonon laser with NV-centers in diamond.

(a)

(b)   (c)
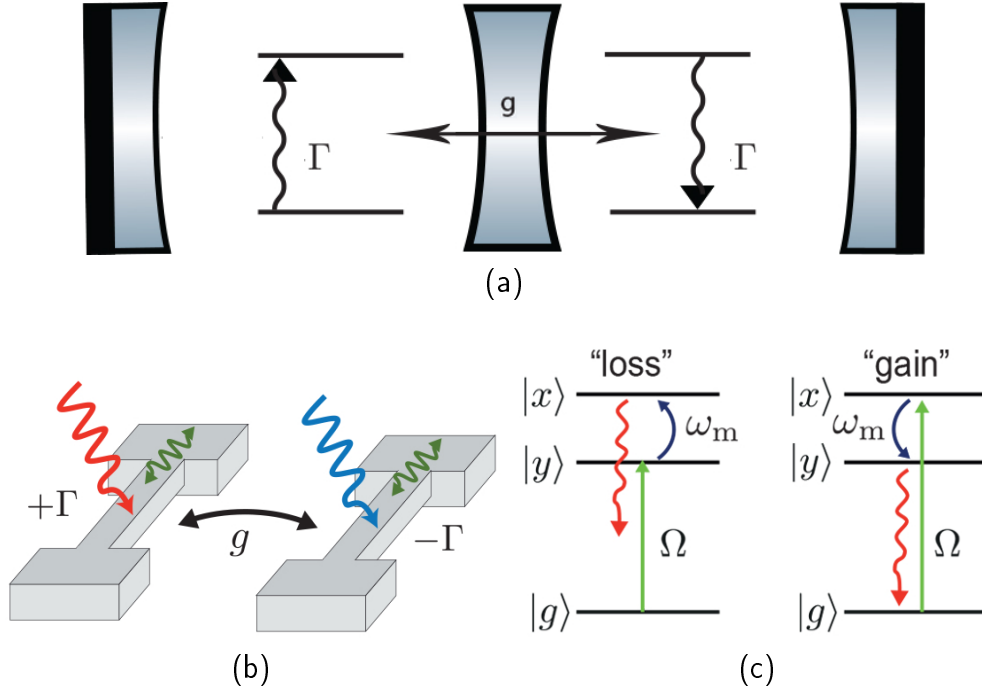
Figure 2.1: a) Setup of two coupled conventional optical lasers, where one is lasing and the other one is cooling. An optical laser can be modeled by an inverted two-level system coupled to a cavity. b) Setup of two coupled phonon lasers, i.e. mechanical resonators with optically-induced gain and loss. c) Scheme for engineering mechanical gain or loss via an optically-driven three-level defect. Depending on the detuning of the pump (green arrow), phonon induced transitions between the two near-degenerate excited states $|x\rangle$ and $|y\rangle$ lead to a net absorption or emission of phonons of frequency ω_m (taken from [12]).

2.3 $\mathcal{PT}$-symmetric finite dimensional quantum systems

From studies of coupled harmonic oscillators with different gain/loss non-linearities follows that the form of the non-linearity has crucial influence on the $\mathcal{PT}$-symmetry behavior. In the second part of the thesis, we extend our analysis to the most non-linear system namely two-level systems and study finite dimensional coupled two-level systems e.g. spin chains. The spins experience alternating gain and loss Γ and interact with their neighbors with the coupling strength g (Figure 2.2). Moreover an overall damping rate κ is included. The Hamiltonian for this system reads

$$\mathcal{H} = \frac{g}{2} \sum_{n=1}^{N} \left(\sigma_n^+ \sigma_{n+1}^- + \sigma_n^- \sigma_{n+1}^+ \right) \tag{2.15}$$
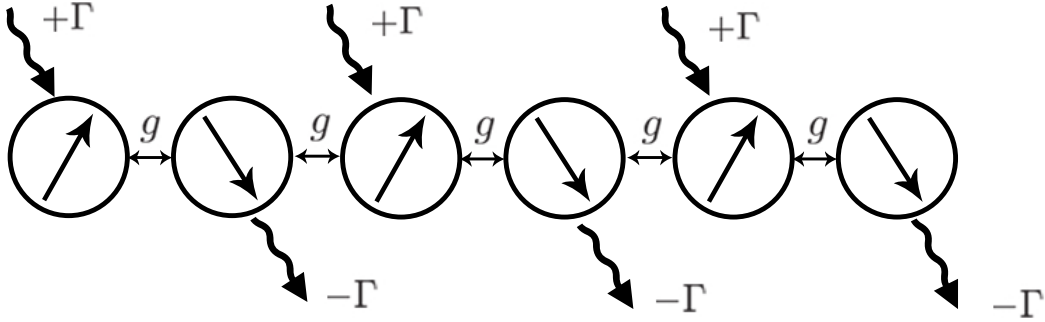
Figure 2.2: Sketch of a spin chain with alternating gain and loss Γ, and coupling strength g.

where σ_n^+ and σ_n^- are the raising and lowering operator for the n-th spin. The master equation of this $\mathcal{PT}$-symmetric system is

$$\dot{\rho} = -\frac{i}{\hbar}[\mathcal{H}, \rho] + \frac{\Gamma}{2}\sum_{n=1}^{N/2}\mathcal{D}[\sigma_{2n-1}^+]\rho + \frac{\Gamma}{2}\sum_{n=1}^{N/2}\mathcal{D}[\sigma_{2n}^-]\rho + \kappa\sum_{n=1}^{N}\mathcal{D}[\sigma_n^-]\rho. \qquad (2.16)$$

The first term describes the time evolution by the Hamiltonian, the second the gain of all odd spins, the third term the loss of all even spins and the last term a small damping on all the spins.

In this master thesis, we develop various numerical methods to solve these master equations (Equation 2.6 and Equation 2.16) in order to investigate $\mathcal{PT}$-symmetry breaking in the quantum regime.

Part I

$\mathcal{PT}$-symmetric oscillators

3 Theoretical Framework

3.1 Master equation in Lindblad form

The master equation [13] describes the time evolution of a system's density operator interacting with a bath. It is assumed that the system-bath interaction is weak and that this interaction does not considerably change the state of the bath (Born approximation). Another assumption is that the bath has very short memory time (Markov approximation). The master equation is trace-preserving and completely positive for any initial condition. The master equation for a simple dissipative system reads

$$\dot{\rho} = -\frac{i}{\hbar}[H, \rho] + \frac{\Gamma}{2}(2a\rho a^\dagger - a^\dagger a\rho - \rho a^\dagger a). \tag{3.1}$$

Here H is the system Hamiltonian, a is the bosonic annihilation operator which describes the coupling to the bath and Γ is the decay rate.

3.2 The Glauber-Sudarshan P-represenation

The coherent state $|\alpha\rangle$ [14] is a quantum mechanical state with minimum uncertainty and the quantum state closest to the classical harmonic oscillator. The coherent state can be obtained by letting the displacement operator $D(\alpha)$ operate on the vacuum state $|0\rangle$,

$$|\alpha\rangle = D(\alpha)|0\rangle. \tag{3.2}$$

In the Fock-basis, the coherent state can be expressed as

$$|\alpha\rangle = e^{-\frac{|\alpha|^2}{2}} \sum_{n=0}^{\infty} \frac{\alpha^n}{\sqrt{n!}}|n\rangle. \tag{3.3}$$

Moreover, it fulfills the following completeness relation

$$1 = \frac{1}{\pi} \int d^2\alpha |\alpha\rangle\langle\alpha|. \tag{3.4}$$

Two coherent states are in general not orthogonal to each other

$$|\langle\beta|\alpha\rangle|^2 = e^{-|\alpha-\beta|^2}. \tag{3.5}$$

The density operator ρ of a pure coherent state is simply $\rho = |\alpha\rangle\langle\alpha|$ and as an extension to arbitrary mixed states we introduce the P-represenation [15]

$$\rho = \int d^2\alpha P(\alpha, \alpha^*)|\alpha\rangle\langle\alpha|, \tag{3.6}$$

where the P-function $P(\alpha, \alpha^*)$ is a real function.
From $\text{Tr}(\rho) = 1$ follows

$$1 = \int d^2\alpha P(\alpha, \alpha^*). \tag{3.7}$$

By using the definition of coherent states in the Fock-basis (Equation 3.3), and the properties of the ladder operator $a|n\rangle = \sqrt{n}|n-1\rangle$ and $a^\dagger|n\rangle = \sqrt{n+1}|n+1\rangle$ one can further derive

$$a|\alpha\rangle\langle\alpha| = \alpha|\alpha\rangle\langle\alpha| \tag{3.8}$$

$$a^\dagger|\alpha\rangle\langle\alpha| = \left(\alpha^* + \frac{\partial}{\partial\alpha}\right)|\alpha\rangle\langle\alpha| \tag{3.9}$$

$$|\alpha\rangle\langle\alpha|a^\dagger = \alpha^*|\alpha\rangle\langle\alpha| \tag{3.10}$$

$$|\alpha\rangle\langle\alpha|a = \left(\alpha + \frac{\partial}{\partial\alpha^*}\right)|\alpha\rangle\langle\alpha|. \tag{3.11}$$

Thus, for a given P- represenation we find:

$$
\begin{aligned}
a^\dagger\rho &= \int d^2\alpha P(\alpha, \alpha^*)\left(\alpha^* + \frac{\partial}{\partial\alpha}\right)|\alpha\rangle\langle\alpha| \\
&= \int d^2\alpha|\alpha\rangle\langle\alpha|e^{-|\alpha|^2}\left(\alpha^* - \frac{\partial}{\partial\alpha}\right)P(\alpha, \alpha^*).
\end{aligned}
\tag{3.12}
$$

where we used integration by parts. Equivalently we can derive

$$
\begin{aligned}
\rho a &= \int d^2\alpha P(\alpha, \alpha^*)\left(\alpha + \frac{\partial}{\partial\alpha^*}\right)|\alpha\rangle\langle\alpha| \\
&= \int d^2\alpha|\alpha\rangle\langle\alpha|e^{-|\alpha|^2}\left(\alpha - \frac{\partial}{\partial\alpha^*}\right)P(\alpha, \alpha^*).
\end{aligned}
\tag{3.13}
$$

Accordingly, we arrive at following operator correspondences:

$$a\rho \leftrightarrow \alpha P(\alpha) \tag{3.14}$$

$$a^\dagger\rho \leftrightarrow \left(\alpha^* - \frac{\partial}{\partial\alpha}\right)P(\alpha) \tag{3.15}$$

$$\rho a \leftrightarrow \left(\alpha - \frac{\partial}{\partial\alpha^*}\right)P(\alpha) \tag{3.16}$$

$$\rho a^\dagger \leftrightarrow \alpha^* P(\alpha). \tag{3.17}$$

We can use these correspondences to transform a master equation (e.g. Equation 3.1) into a differential equation.

Example: Harmonic oscillator coupled to a thermal bath

The corresponding master equation reads

$$\dot{\rho} = -i\omega[a^\dagger a, \rho] + \frac{\Gamma}{2}(N_{th}+1)(2a\rho a^\dagger - a^\dagger a\rho - \rho aa) + \frac{\Gamma}{2}N_{th}(2a^\dagger \rho a - aa^\dagger \rho - \rho aa^\dagger) \tag{3.18}$$

where ω is the harmonic oscillator's frequency, Γ the rate of energy exchange with the thermal bath and $N_{th} = (e^{\hbar\omega/k_B T} - 1)^{-1}$ the thermal occupation number. While the second term describes the loss to the environment, the third term describes the gain.

The corresponding differential equation for the P-function is

$$\frac{\partial P(\alpha, \alpha^*)}{\partial t} = \left[\left(\frac{\Gamma}{2} + i\omega \right) \frac{\partial}{\partial \alpha}\alpha + \left(\frac{\Gamma}{2} - i\omega \right) \frac{\partial}{\partial \alpha^*}\alpha^* + \Gamma N_{th}\frac{\partial^2}{\partial \alpha \partial \alpha^*} \right] P(\alpha, \alpha^*). \tag{3.19}$$

This partial differential equation of 2nd order is called Fokker-Planck equation [16].

3.3 Fokker-Planck equation

The Fokker-Planck equation is a partial differential equation that describes the time evolution of a probability density function and can be used to explain several physical systems e.g. the Brownian motion where the time evolution of a particle under the influence of a stochastic force is described. A general Fokker-Planck equation in n variables may be written as

$$\frac{\partial P(x, t)}{\partial t} = \left[-\frac{\partial}{\partial x_j}A_j(x) + \frac{1}{2}\frac{\partial}{\partial x_i}\frac{\partial}{\partial x_j}D_{ij}(x) \right] P(x, t). \tag{3.20}$$

The first derivative term determines the mean or deterministic motion and is therefore often called drift term, while the second derivative term is called diffusion term, because it causes broadening or diffusion of $P(x, t)$ if it is positive definite. Further insight into the effects of those two terms can be gained by looking at the equations of motion for the expectation values

$$\frac{d\langle x_k \rangle}{dt} = \langle A_k \rangle, \tag{3.21}$$

$$\frac{d\langle x_k x_l \rangle}{dt} = \langle x_k A_l \rangle + \langle x_l A_k \rangle + \frac{1}{2}\langle D_{kl} + D_{lk} \rangle . \tag{3.22}$$

We see that the diffusion does not contribute to the linear, but to the quadratic expectation values.

For a harmonic oscillator coupled to a thermal bath (Equation 3.18) we get:

$$\frac{d\langle \alpha \rangle}{dt} = -(i\omega + \frac{\Gamma}{2})\langle \alpha \rangle \tag{3.23}$$

$$\frac{d\langle |\alpha|^2 \rangle}{dt} = -\Gamma\langle |\alpha|^2 \rangle + \Gamma N_{th} = -\Gamma(\langle |\alpha|^2 \rangle - N_{th}). \tag{3.24}$$

In the last line we can see that the occupation number of the harmonic oscillator $|\alpha|^2$ reaches the occupation of the thermal bath in steady state $|\alpha|^2 = N_{th}$.

3.3.1 Steady state solution

For many problems it is sufficient to know the steady state solution. In the steady state, we set the time derivative in Equation 3.20 to zero resulting in

$$\frac{\partial}{\partial x_i}\left[-A_i(x)P(x) + \frac{1}{2}D_{ij}(x)P(x) \right] = 0. \tag{3.25}$$

This equations holds if we find a solution that obeys

$$A_i(x)P(x) = \frac{1}{2}\frac{\partial}{\partial x_j}\left[D_{ij}(x)P(x) \right], \tag{3.26}$$

which implies

$$D_{ij}\frac{\partial \ln P}{\partial x_j} = 2A_i(x) - \frac{\partial D_{jk}(x)}{\partial x_k}. \tag{3.27}$$

With the Ansatz $P(x) = e^{-\phi(x)}$ we get

$$-\frac{\partial \phi(x)}{\partial x_i} = 2(D^{-1})_{ij}\left[A_j(x) - \frac{1}{2}\frac{\partial D_{jk}}{\partial x_k} \right] =: F_i. \tag{3.28}$$

This set of equations can only be solved simultaneously if the so called potential conditions are satisfied

$$-\frac{\partial^2 \phi}{\partial x_i \partial x_j} = \frac{\partial F_j}{\partial x_i} = \frac{\partial F_i}{\partial x_j} = -\frac{\partial^2 \phi}{\partial x_i \partial x_j}. \tag{3.29}$$

The P-function of a harmonic oscillator coupled to a thermal bath in steady state reads

$$P(\alpha, \alpha^*) = \frac{1}{\pi N_{th}}e^{-\frac{|\alpha|^2}{N_{th}}}. \tag{3.30}$$

It is a Gaussian distribution centered around $|\alpha| = 0$ with a variance proportional to N_{th}. In general, the Fokker-Planck equation is difficult to solve analytically even in the steady state case. The best way to solve it numerically is to map the Fokker-Planck equation to a stochastic differential equation.

3.4 Stochastic differential equation (SDE)

A Fokker-Planck equation of the form Equation 3.20 can be written in a completely equivalent form as a Langevin equation [17]

$$\frac{dx}{dt} = A(x,t) + B(x,t)\xi(t),$$ (3.31)

where $B(x,t)B(x,t)^T = D(x,t)$ and $\xi(t)$ are fluctuating forces with zero mean $\langle \xi(t) \rangle = 0$ and the correlations vanish at different times

$$\langle \xi_i(t)\xi_j(t') \rangle = \delta_{ij}\delta(t-t').$$ (3.32)

The spectrum of the delta correlated noise process is a constant, therefore this is often stated as white noise. Furthermore, we may introduce the Wiener process

$$dW(t) \equiv W(t+\Delta t) - W(t) = \int_t^{t+dt} \xi(s)ds.$$ (3.33)

The Wiener process is a stochastic process with Gaussian increments with zero mean and variance $\sigma^2 = t - s$

$$W(t) - W(s) = N(0, t-s).$$ (3.34)

From Equation 3.32 and Equation 3.33 it follows that

$$\langle dW_i dW_j \rangle = \delta_{ij}dt.$$ (3.35)

3.4.1 Ito stochastic differential equation

A stochastic quantity $x(t)$ obeys an Ito stochastic differential equation [17] written as

$$dx(t) = a[x(t),t]dt + b[x(t),t]dW(t)$$ (3.36)

if for all t and t_0,

$$x(t) = x(t_0) + \int_{t_0}^t a[x(t'),t']dt' + \int_{t_0}^t b[x(t'),t']dW(t').$$ (3.37)

Consider an arbitrary function $f[x(t)]$. Deviating from the ordinary calculus, stochastic Ito differential equations have to be expanded up to the second order in dW, thus

$$df(x) = \frac{\partial f(x)}{\partial x}dx + \frac{1}{2}\frac{\partial^2 f(x)}{\partial x^2}dx^2.$$ (3.38)

This is well known as Ito's Lemma. We now consider the time evolution of the expectation value of an arbitrary $f[x(t)]$ using the formula above

$$\frac{d}{dt}\langle f[x(t)]\rangle = \left\langle a[x(t),t]\frac{\partial f}{dx} + \frac{1}{2}b[x(t),t]^2\frac{\partial^2 f}{\partial x^2}\right\rangle. \tag{3.39}$$

We introduce a normalized probability distribution $P(x,t)$, which can be used to calculate expectation values $\langle x(t)\rangle = \int xP(x,t)dx$. We can rewrite Equation 3.39 as

$$\frac{d}{dt}\langle f[x(t)]\rangle = \int dx f(x)\frac{\partial P(x,t)}{\partial t} = \int dx\left[a(x,t)\frac{\partial f}{\partial x} + \frac{1}{2}b(x,t)^2\frac{\partial^2 f}{\partial x^2}\right]P(x,t). \tag{3.40}$$

After integration by parts we obtain

$$\int dx f(x)\frac{\partial P(x,t)}{\partial t} = \int dx f(x)\left[-\frac{\partial}{\partial x}a(x,t) + \frac{1}{2}\frac{\partial^2}{\partial x^2}b(x,t)^2\right]P(x,t). \tag{3.41}$$

Since this is for an abitrary $f(x)$ we see that

$$\frac{\partial P(x,t)}{\partial t} = \left[-\frac{\partial}{\partial x}a(x,t) + \frac{1}{2}\frac{\partial^2}{\partial x^2}b(x,t)^2\right]P(x,t). \tag{3.42}$$

By comparison with the Fokker-Planck equation (Equation 3.20) one finds

$$a(x,t) = A(x,t) \text{ and } b(x,t)^2 = D(x). \tag{3.43}$$

Generalizing the above result to arbitrary dimensions we find

$$\vec{a}(x,t) = \vec{A}(x,t) \text{ and } \mathbf{D}(x) = \mathbf{B}^T(x)\mathbf{B}(x). \tag{3.44}$$

Thus, $\mathbf{B}(x)$ can be derived from $\mathbf{D}(x)$ by taking the square root $\mathbf{B}(x) = \sqrt{\mathbf{D}(x)}$.

3.4.2 Stratonovich stochastic differential equation

The definition of the Stratonovich integral is such as to make the ordinary rules of the calculus valid for change of variables as opposed to Equation 3.38

$$(S)\ df[x(t)] = \frac{\partial f(x)}{\partial x}dx. \tag{3.45}$$

As a consequence, a function has to be evaluated at $x = \frac{1}{2}(x_{j+1} - x_j)$ when integrating the Stratonovich stochastic differential equation. For further insight we write a simple Stratonovich SDE

$$(S)\ dx = b(x,t)dW(t) \tag{3.46}$$

in discretized form as

$$x_{i+1} = x_i + b[\frac{1}{2}(x_{i+1} + x_i)](W_{i+1} - W_i). \tag{3.47}$$

The Ito SDE
$$dx = adt + bdW \tag{3.48}$$

can be equivalently written in Stratonovich form

$$(S)\ dx = \left(a - \frac{1}{2}b\frac{\partial b}{\partial x}\right)dt + bdW. \tag{3.49}$$

Similarly, the Stratonovich SDE

$$(S)\ dx = \alpha dt + \beta dW \tag{3.50}$$

can be written in Ito form

$$dx = \left(\alpha + \frac{1}{2}\beta\frac{\partial \beta}{\partial x}\right)dt + \beta dW. \tag{3.51}$$

If the diffusion b is constant, the Ito and Stratonovich form are identical.

4 Numerical implementations

4.1 Stochastic Schrödinger equation/ quantum trajectories

Quantum trajectories is a method which, much like the master equation, describes small open quantum systems coupled to a large reservoir but it operates on the wave-function rather than using a density matrix [18]. The idea is to let the system evolve with an effective Hamiltonian, where at each time step, a quantum jump (discontinuity) may take place with some probability or not. A quantum jump could for example be a cavity losing one photon to the bath. The big advantage of quantum trajectories is that for a state vector with n elements, only n elements have to be computed while by using the master equation a density matrix with n^2 elements has to be computed.

There are mainly two ways to implement quantum trajectories in a computer program. One is to calculate the probability of a jump for every time step and then choose a random number to determine if a jump occurs or not. Another way is to let the state evolve until the norm of the state equals the chosen random number and then a jump happens for sure. This is in general more effective and will be discussed in more detail in the following section.

4.2 Algorithm for one trajectory

1. Choose inital state $|\psi(0)\rangle$.

2. Choose random number $r \in [0, 1]$.

3. Time evolution with the non-Hermitian effective Hamiltonian $\mathcal{H}_{eff}$ until $r > \langle\psi(t)|\psi(t)\rangle$. $\mathcal{H}_{eff}$ for a simple dissipative system (see Equation 3.1) can be derived from

$$\dot{\rho} = -\frac{i}{\hbar}[\mathcal{H}, \rho] + \frac{\Gamma}{2}\mathcal{D}[c] = -\frac{i}{\hbar}\mathcal{H}_{eff}\rho + \frac{i}{\hbar}\rho\mathcal{H}_{eff}^{\dagger} + \Gamma c\rho c^{\dagger} \qquad (4.1)$$

where $\mathcal{H}_{eff} = \mathcal{H} - i\frac{\Gamma}{2}c^{\dagger}c$.

4. Quantum jump and normalization $|\psi\rangle = \frac{c|\psi\rangle}{\langle\psi|c^\dagger c|\psi\rangle}$.
   Note: If the system has N jump operators c_i, the probability which quantum jump happens is computed by $p_i = \frac{\langle\psi|c_i^\dagger c_i|\psi\rangle}{\sum_{i=0}^{N}\langle\psi|c_i^\dagger c_i|\psi\rangle}$.

5. Go to 2. until $t = t_{end}$.

To get the same trajectory as by solving the master equation, hundreds of trajectories have to be calculated and averaged. The relative error goes with $\frac{1}{\sqrt{n_{traj}}}$ where n_{traj} is the number of trajectories. Because the quantum jumps appear at random times, it is recommended to interpolate the data to a discrete grid before averaging.

There are several ways to do point 3 (the time evolution):

- Solving the Schrödinger equation via Runge-Kutta method. The standard Runge-Kutta algorithm is a fourth order method and needs four function calls for fixed discrete time steps and eleven function calls for every two steps by the use of adaptive time steps. In Matlab solving an ordinary differential equation with Runge-Kutta and adaptive time steps can be easily done by using the ODE45 function.

- Calculating the time evolution operator $U = e^{-iH_{eff}\Delta t}$ for one time step. As H_{eff} does not depend on time, this has to be done only once and time evolution of a state can be done by simple multiplication $|\psi(t + \Delta t)\rangle = U|\psi(t)\rangle$. One difficulty is to find the right time step size. It can be approximated by setting the time step to the inverse of the norm of the Hamiltonian matrix $\Delta t \approx 1/\|H_{eff}\|_2$. The other difficulty is to compute the exponential of a large matrix. There are several options to calculate the exponential of a large matrix:

  - Pade Approximation
  - Diagonalization of the Matrix
  - Taylor series

  In this work the Pade Aproximation is used as it is fast and accurate. It is the standard implementation of a matrix exponential in Matlab and can easily be adapted for sparsed matrices. Calculating the exponential by diagonalizing the matrix is only recommended for small matrices, but doesn't work for really big matrices with > 40000 dimensions on an ordinary computer. Taylor series uses the least memory but the results seem to fail for certain matrices when time-steps are large.

By solving the master equation only states with 400 elements can be computed, while states with more than 100000 elements can be calculated by solving the stochastic Schrödinger equation via the time evolution operator on an ordinary computer. Note: the master equation only has to be solved once while the stochastic Schrödinger has to be solved and averaged hundreds of times.

4.3 Stochastic differential equations

4.3.1 Stochastic Euler method

The simplest numerical method to solve a stochastic Ito differential equation (see subsection 3.4.1) such as

$$dx = a(x,t)dt + b(x,t)dW \tag{4.2}$$

is by the stochastic Euler method, which is an extension of the Euler method for odinary differential equations (ODE). Equation 4.2 can be solved by the stochastic Euler method (often called Euler-Maruyama method):

$$x_{n+1} = x_n + a(x_n, t_n)\Delta t + b(x_n, t_n)\Delta W_n. \tag{4.3}$$

The random increment is computed as

$$\Delta W_n = \sqrt{\Delta t} z_i \tag{4.4}$$

where z_i is chosen from N(0,1). The local truncation error in each time step of the Euler-Maruyama method is $\mathcal{O}(\Delta t)$, much worse than the deterministic Euler method, essentially due to the stochastic term.
The dominant error will thus be random and uncorrelated, so we consider the error in a random walk of N steps of mean size of order t/N, which will scale as $\sqrt{N}(t/N) = t/\sqrt{N} = \mathcal{O}(\Delta t^{1/2})$. Thus the global error of the stochastic Euler scheme converges very badly, as $\mathcal{O}(\Delta t^{1/2})$. This can be improved by using the Milstein method.

4.3.2 Milstein method

An stochastic Ito differential equation Equation 4.2 can be solved numerically by the Milstein method:

$$x_{n+1} = x_n + a(x_n, t_n)\Delta t + b(x_n, t_n)\Delta W_n + \frac{1}{2}b(x_n, t_n)b'(x_n, t_n)(\Delta W_n^2 - \Delta t) \tag{4.5}$$

where the local truncation error is $\mathcal{O}(\Delta t^{3/2})$ and by using the same reasoning as above the global error is again by a factor $\Delta t^{1/2}$ larger and thus $\mathcal{O}(\Delta t)$.

4.3.3 Stochastic Runge-Kutta method

An $\mathcal{O}(\Delta t)$ stochastic Runge-Kutta method of comparable accuracy to the Milstein method is

$$d_n = x_n + a(x_n, t_n)\Delta t + b(x_n, t_n)\sqrt{\Delta t}$$

$$x_{n+1} = x_n + a(x_n, t_n)\Delta t + b(x_n, t_n)\Delta W_n + \frac{1}{2\sqrt{\Delta t}}[b(d_n, t_{n+1}) - b(x_n, t_n)][\Delta W_n^2 - \Delta t].$$

$$\tag{4.6}$$

There are also higher order methods than a $\mathcal{O}(\Delta t^{3/2})$ method, but these methods are substantially more complicated. In general it is recommendable to use higher order methods than the Euler-Maruyama method, because the most time consuming part in the calculation is the generation of normally distributed random numbers. Comparison of different methods for our specific problems showed that there is no significant difference in accuracy between the different methods. Thus, we used the Euler-Maruyama method to numerically solve stochastic differential equations (see section 5.2).

In order to get good results for various expectation values, the stochastic differential equation has to be solved thousands of times. Instead of evolving one equation from t_0 to t_{end} it is highly recommended to do the time evolution for thousands of equations simultaneously [19] which can be easily implemented in Matlab. Tests have shown that this results in a speed-up of a factor 300.

5 Results and Discussion

5.1 Quantum trajectories

A simple $\mathcal{PT}$-symmetric system consists of two coupled oscillators where one oscillator is heated and the other one cooled. For such a system the master equation reads

$$\dot{\rho} = -\frac{i}{\hbar}[\mathcal{H}, \rho] + \frac{\Gamma}{2}\mathcal{D}[c_1^\dagger]\rho + \frac{\Gamma}{2}\mathcal{D}[c_2]\rho \tag{5.1}$$

with the Lindblad superoperator

$$\mathcal{D}[c]\rho \equiv 2c\rho c^\dagger - c^\dagger c\rho - \rho c^\dagger c \tag{5.2}$$

and the Hamiltonian is given by

$$\mathcal{H} = \hbar\omega_c c_1^\dagger c_1 + \hbar\omega_c c_2^\dagger c_2 + \hbar g(c_1^\dagger c_2 + c_1 c_2^\dagger) \tag{5.3}$$

where ω_c is the oscillators frequency, g is the coupling strength between the two oscillators, c and $c^\dagger$ are the bosonic annihilation and creation operators. By moving into a rotated frame with respect to ω_c and calculating the time evolution of the expectation values of c_1 and c_2 we get

$$\begin{pmatrix} \langle \dot{c}_1 \rangle \\ \langle \dot{c}_2 \rangle \end{pmatrix} = \begin{pmatrix} \frac{\Gamma}{2} & -ig \\ -ig & -\frac{\Gamma}{2} \end{pmatrix} \begin{pmatrix} \langle c_1 \rangle \\ \langle c_2 \rangle \end{pmatrix}. \tag{5.4}$$

By comparing this equation with the Schrödinger equation $|\dot{\psi}\rangle = -iH|\psi\rangle$ one arrives at a $\mathcal{PT}$-symmetric Hamiltonian

$$H = \begin{pmatrix} i\frac{\Gamma}{2} & g \\ g & -i\frac{\Gamma}{2} \end{pmatrix}. \tag{5.5}$$

We can define two regimes, the $\mathcal{PT}$-symmetric regime with real eigenvalues and the $\mathcal{PT}$-broken regime with complex eigenvalues. In the symmetric regime, the state will just oscillate in the complex plane, while in the broken regime, the occupation of one oscillator will blow up and the occupation of the other one will be depleted. In order to get a finite occupation in steady state, there has to be some non-linearity, since even with an overall linear loss κ, the occupation will either go to infinity/zero or there will just be oscillations.

To obtain finite occupation in steady state we therefore write a general master equation

$$\dot{\rho} = -\frac{i}{\hbar}[\mathcal{H}, \rho] + \frac{\Gamma}{2}\mathcal{D}[c_g^\dagger]\rho + \frac{\Gamma}{2}\mathcal{D}[c_l]\rho \tag{5.6}$$

with the same Hamiltonian as before (Equation 5.3) but with effective ladder operator for gain

$$c_g^\dagger = c_1^\dagger \sqrt{f(n_1)} \tag{5.7}$$

and loss

$$c_l = \sqrt{f(n_2)} c_2 \tag{5.8}$$

where $f(n_i)$ is an arbitrary function only depending on $n_i = c_i^\dagger c_i$. The equations of motion for the occupation expectation value read

$$\frac{d\left\langle c_1^\dagger c_1 \right\rangle}{dt} = -ig(\left\langle c_1^\dagger c_2 \right\rangle - \left\langle c_1 c_2^\dagger \right\rangle) + \Gamma \left\langle (1 + c_1^\dagger c_1) f(n_1) \right\rangle, \tag{5.9}$$

$$\frac{d\left\langle c_2^\dagger c_2 \right\rangle}{dt} = ig(\left\langle c_1^\dagger c_2 \right\rangle - \left\langle c_1 c_2^\dagger \right\rangle) - \Gamma \left\langle c_2^\dagger f(n_2) c_2 \right\rangle, \tag{5.10}$$

$$\frac{d\left\langle c_1^\dagger c_1 + c_2^\dagger c_2 \right\rangle}{dt} = \Gamma \left\langle (1 + c_1^\dagger c_1) f(n_1) \right\rangle - \Gamma \left\langle c_2^\dagger f(n_2) c_2 \right\rangle. \tag{5.11}$$

Although there are many possibilities for the non-linear function $f(n)$, we will focus on functions of the form

$$f(n) = \frac{1}{\left(1 + \frac{c^\dagger c}{n_0}\right)^\nu} \tag{5.12}$$

where n_0 is the saturation parameter. The saturation parameter n_0 determines the occupation in steady state and as a results denotes how quantum or classical a system is. A saturation $n_0 \approx 1$ can be referred to the quantum regime while a $n_0 \gg 1$ can be seen as the classical regime.

The form of the non-linear function is motivated by the form of the conventional optical laser equation ($\nu = 1$) and the phonon laser ($\nu = 2$).

5.1.1 $\nu = 1$

We first focus on the case of a non-linear function with $\nu = 1$ which can be referred to as a conventional optical laser Figure 2.1a.

In this case the non-linear function reads

$$f(n) = \frac{1}{1 + \frac{c^\dagger c}{n_0}} \tag{5.13}$$

and the effective ladder operators for gain and for loss are

$$c_g^\dagger = c_1^\dagger \frac{1}{\sqrt{1 + \frac{c_1^\dagger c_1}{n_0}}} \tag{5.14}$$

and

$$c_l = \frac{1}{\sqrt{1 + \frac{c_2^\dagger c_2}{n_0}}} c_2. \tag{5.15}$$

As stated before, we are interested in the steady state behavior of the $\mathcal{PT}$-symmetric system. We assume that in steady state there may be some oscillation of occupation between the two cavities, but there should not be any change of the sum of the occupation numbers $\left\langle c_1^\dagger c_1 + c_2^\dagger c_2 \right\rangle$. Thus, we look at Equation 5.11 to check if the time dependence can vanish:

$$\frac{d \left\langle c_1^\dagger c_1 + c_2^\dagger c_2 \right\rangle}{dt} = \Gamma \left\langle \frac{1 + c_1^\dagger c_1}{1 + \frac{c_1 c_1}{n_0}} \right\rangle - \Gamma \left\langle c_2^\dagger \frac{1}{1 + \frac{c_2^\dagger c_2}{n_0}} c_2 \right\rangle. \tag{5.16}$$

To get a clearer picture, we expand the wave function into its Fock eigenstates $|\Psi\rangle = \sum_{n=0}^{\infty} a_n |n\rangle \otimes \sum_{m=0}^{\infty} b_m |m\rangle$

$$\frac{d \left\langle c_1^\dagger c_1 + c_2^\dagger c_2 \right\rangle}{dt} = \Gamma \left(|a_0|^2 + \sum_{n=1}^{\infty} |a_n|^2 \frac{1 + n}{1 + \frac{n}{n_0}} - \sum_{m=1}^{\infty} |b_m|^2 \frac{m}{1 + \frac{m-1}{n_0}} \right) \tag{5.17}$$

In the $\mathcal{PT}$-symmetric regime, both cavities should be equally populated $\left\langle c_1^\dagger c_1 \right\rangle \approx \left\langle c_2^\dagger c_2 \right\rangle$ and if we assume that the population of the Fock states follow a normal or poissonian distribution a finite steady state can only be reached in the case of $n_0 = 1$ if the ground state of the first cavity is depleted while for $n_0 > 1$ a finite steady state can not be reached even if the ground state is depleted. Therefore, we include an overall damping κ. The master equation now reads

$$\dot{\rho} = -\frac{i}{\hbar}[\mathcal{H}, \rho] + \frac{\Gamma}{2}\mathcal{D}[c_g^\dagger]\rho + \frac{\Gamma}{2}\mathcal{D}[c_l]\rho + \kappa(\mathcal{D}[c_1]\rho + \mathcal{D}[c_2]\rho). \tag{5.18}$$

We can numerically solve the master equation of this system by the quantum trajectory method (see section 4.1). For $n_0 = 1$, which can be referred as the quantum regime we can identify that for low Γ/g the mean values of the occupations coincides while for $\Gamma/g > 15$ the cavity with non-linear gain is slightly higher populated than the cavity with linear loss (Figure 5.1). Although the occupation differs slightly, its variances remain the same and both grow with the occupation. Moreover, there are not any differences in the current

$$\langle j \rangle = i \left\langle c_1 c_2^\dagger - c_1^\dagger c_2 \right\rangle \tag{5.19}$$
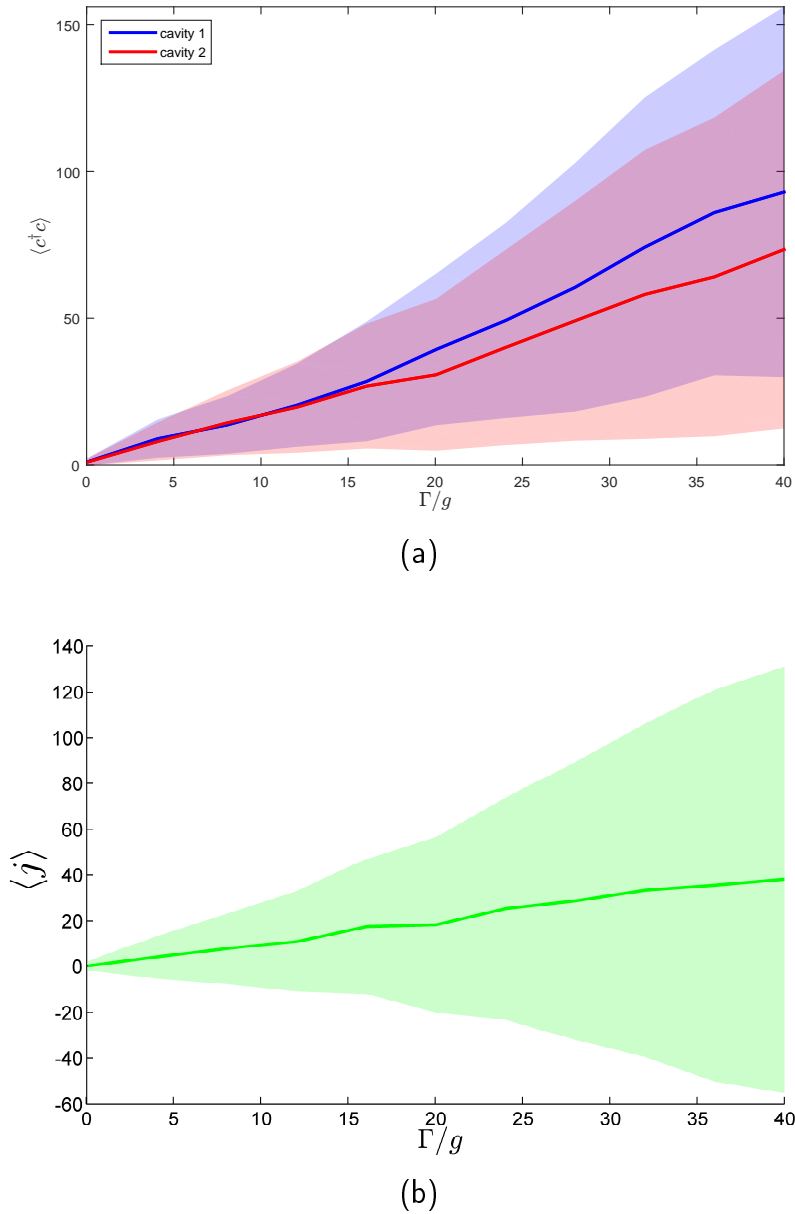
(a)

(b)

Figure 5.1: a) The average steady state occupation number of two coupled cavities where one experiences non-linear gain with $\nu = 1$ and the other the same amount of non-linear loss with $\nu = 1$ in the quantum regime is plotted as function of Γ/g, the ratio between gain/loss and the coupling between the cavities. We can clearly see for higher Γ/g than 15 the average occupation of the two cavities begin to differ, but no other fundamental changes can be observed. The variance of the occupation depends linearly on the occupation and this phenomenon holds true in both regions where the average occupation is the same and where it differs. b) The current between the cavities in steady state as a function of Γ/g is plotted. The expectation value of the current and its variance grows for higher Γ/g. We cannot identify any difference between both regions. We can therefore conclude that the phase is only weakly broken. These are the results of a quantum trajectory simulation with an overall damping $\kappa = 0.01g$ and a photon saturation number of $n_0 = 1$, which can be refered to the quantum regime. Each cavity consisted of 200 Fock states and 1000 trajectories were calculated and averaged.
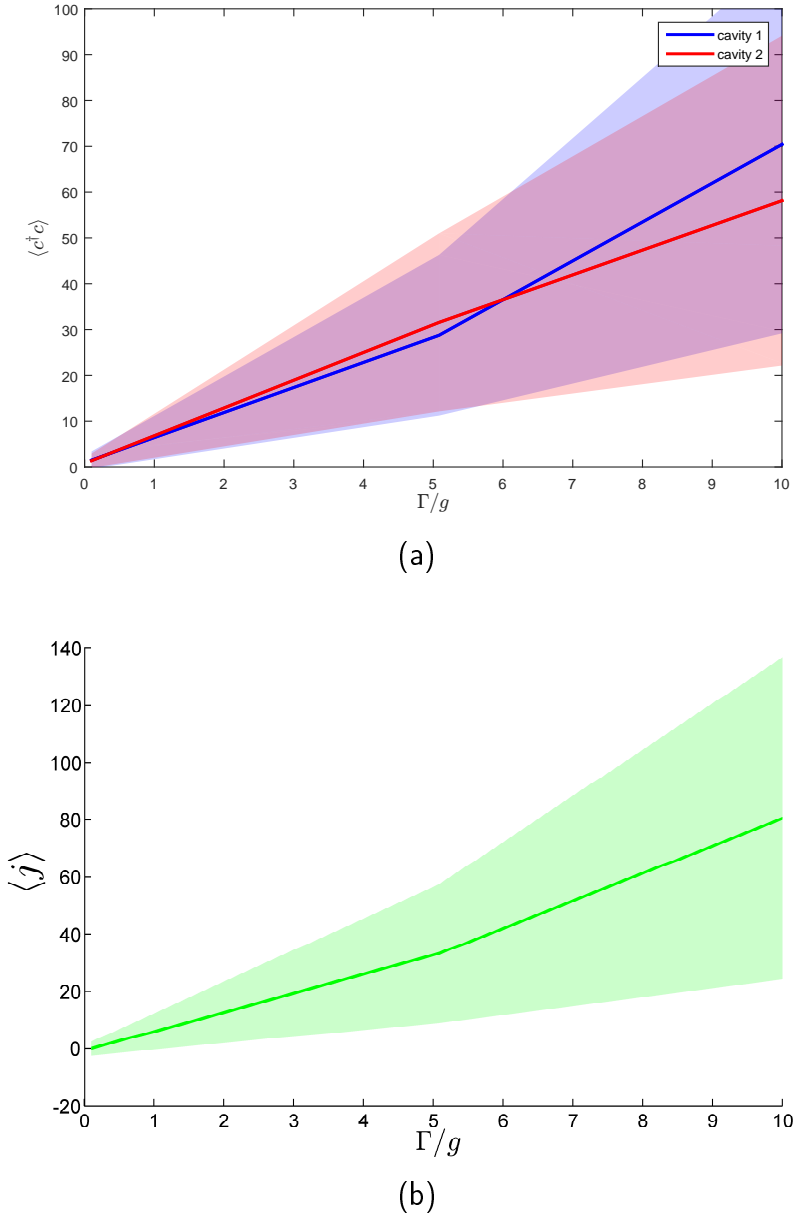
(a)

(b)

Figure 5.2: a) The average occupation in steady state of both cavities with non-linear gain/loss with $\nu = 1$ as a function of Γ/g in the almost classical regime with a photon saturation number of $n_0 = 10$. We can identify a region of low Γ/g where the expectation value of the occupation of the two cavities coincide, while for $\Gamma/g > 6$ the averages of the occupation differ. Although the the occupation differs, its variances stay approximately the same. b) The steady state current between the two cavities as a function of Γ/g is plotted. The expectation value of the current and its variance grows for higher Γ/g. We cannot identify any difference between both regions. Apart from changes in the average occupation number, no significant changes can be observed. Therefore we conclude that the phase is only weakly broken. These are the result of a quantum trajectory simulation with an overall damping $\kappa = 0.01g$. Each cavity consisted of 180 Fock states and 1000 trajectories were calculated and averaged.
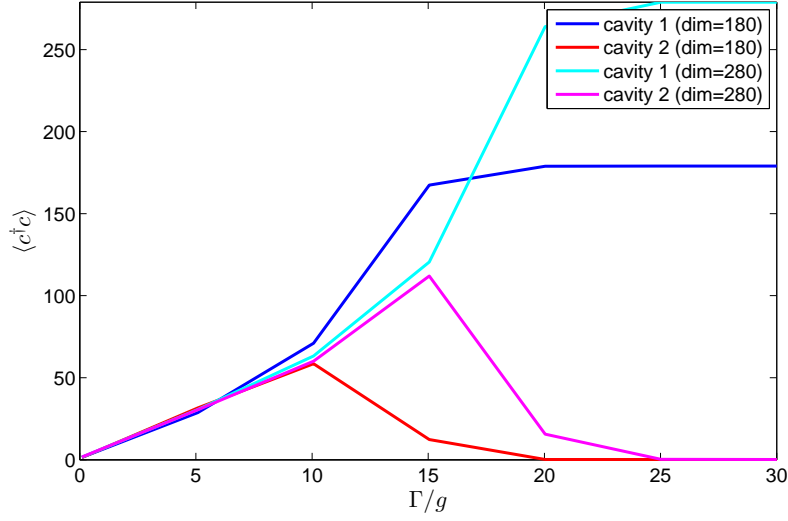
Figure 5.3: a) The average occupation of both cavities with non-linear gain/loss with $\nu = 1$ in steady state as function of Γ/g in the almost classical regime with a photon saturation number of $n_0 = 10$. In these quantum trajectory calculations each cavity consisted of 180 and 280 Fock states. In contrast to Figure 5.2 calculations were performed for higher Γ/g. We can observe a phase transition, but most likely only because of the inclusion of only a limited number of states in our numerical calculations. While the transition point moves from $\Gamma/g = 10$ to $\Gamma/g = 15$ by allowing 100 additional Fock states in each cavity, we can assume that the transition vanishes for an infinite Hilbert space. Again the quantum trajectory simulations were performed by including an overall damping of $\kappa = 0.01g$ and around 1000 trajectories were calculated to obtain this result.

between the two regimes. The current and the variances of the current increase for higher Γ/g. From this we can conclude that the $\mathcal{PT}$-symmetry is only weakly broken and no phase transition is observed.

The mean occupation scales approximately with n_0 making a proper numerical analysis for $n_0 = 10$ more difficult, as the limit of a Hilbert space of nearly 100000 states is reached even for significantly lower Γ/g.

In the case of $n_0 = 10$, the (almost) classical regime, we identify a similar behavior as in the quantum regime (see Figure 5.2). For low Γ/g, the mean occupation coincides while for higher Γ/g the expectation value of the occupations slightly differs, but the basic physics remains the same.

In Figure 5.3 we extended our analysis to even higher Γ/g. We observe a phase transition, which can be attributed to the inclusion of only a limited number of state in our calculations. While the transition point moves from $\Gamma/g = 10$ to $\Gamma/g = 15$ by allowing 100 additional Fock states in each cavity, we can assume that

the transition vanishes for an infinite Hilbert space. To clarify this assumption, other methods as constructing and simulating stochastic differential equation for this problem need to be applied. This will be done in the following chapter.

5.1.2 $\nu = 2$

We will now focus on the system with a non-linear function with $\nu = 2$ where a possible implementation is a phonon laser with NV-centers in diamond. In this case, the non-linear function reads

$$f(n) = \frac{1}{(1 + \frac{c^\dagger c}{n_0})^2} \tag{5.20}$$

and the effective ladder operators are

$$c_g^\dagger = c_1^\dagger \frac{1}{1 + \frac{c_1^\dagger c_1}{n_0}} \tag{5.21}$$

and

$$c_l = \frac{1}{1 + \frac{c_2^\dagger c_2}{n_0}} c_2. \tag{5.22}$$

Again, we check if a steady state exists by using the arguments used before and looking at the time evolution of the sum of both occupation numbers.

$$\frac{d \left\langle c_1^\dagger c_1 + c_2^\dagger c_2 \right\rangle}{dt} = \Gamma \left\langle \frac{1 + c_1^\dagger c_1}{(1 + \frac{c_1 c_1}{n_0})^2} \right\rangle - \Gamma \left\langle c_2^\dagger \frac{1}{(1 + \frac{c_2^\dagger c_2}{n_0})^2} c_2 \right\rangle \tag{5.23}$$

To get a clearer picture, we expand the wave function into its Fock eigenstates $|\Psi\rangle = \sum_{n=0}^{\infty} a_n |n\rangle \otimes \sum_{m=0}^{\infty} b_m |m\rangle$

$$\frac{d \left\langle c_1^\dagger c_1 + c_2^\dagger c_2 \right\rangle}{dt} = \Gamma \left(|a_0|^2 + \sum_{n=1}^{\infty} |a_n|^2 \frac{1+n}{(1 + \frac{n}{n_0})^2} - \sum_{m=0}^{\infty} |b_m|^2 \frac{m}{(1 + \frac{m-1}{n_0})^2} \right) \tag{5.24}$$

If we assume a normal distribution of Fock states, we can conclude that if $\left\langle c_1^\dagger c_1 \right\rangle \approx \left\langle c_2^\dagger c_2 \right\rangle$ as well as if $\left\langle c_1^\dagger c_1 \right\rangle > \left\langle c_2^\dagger c_2 \right\rangle$ a steady state exists even without a linear overall loss of the cavities. Nevertheless a finite overall loss κ is added in order to reduce the amount of time steps needed to reach steady state.

Quantum trajectory simulations with an overall damping $\kappa = 10^{-4} g$ in the quantum regime $n_0 = 1$ show that for low Γ/g the two coupled systems are on average equally distributed and the system is $\mathcal{PT}$-symmetric (Figure 5.4). For $\Gamma/g > 24$ the states begin to differ, a phase transition occurs. In the symmetric regime the variance of the occupation number grows with the occupation and reaches its maximum at the transition point $\Gamma/g > 24$. While in the symmetric regime the variance is quite large, for high Γ/g in the broken regime the variance is again low and
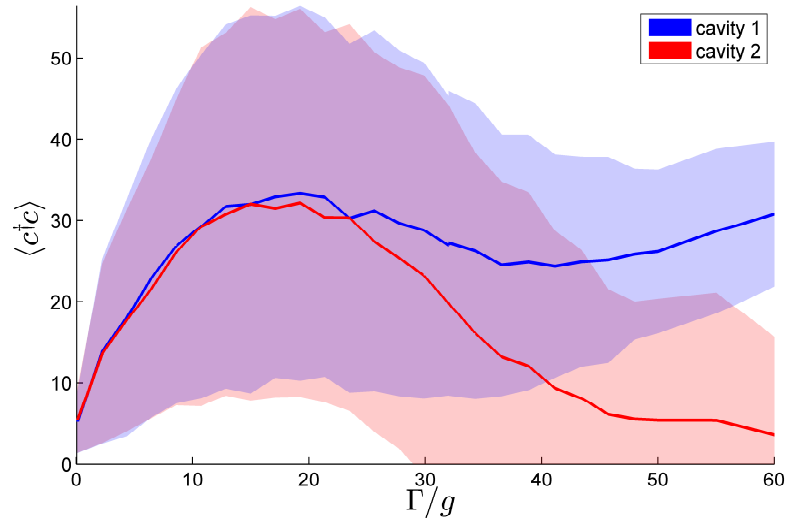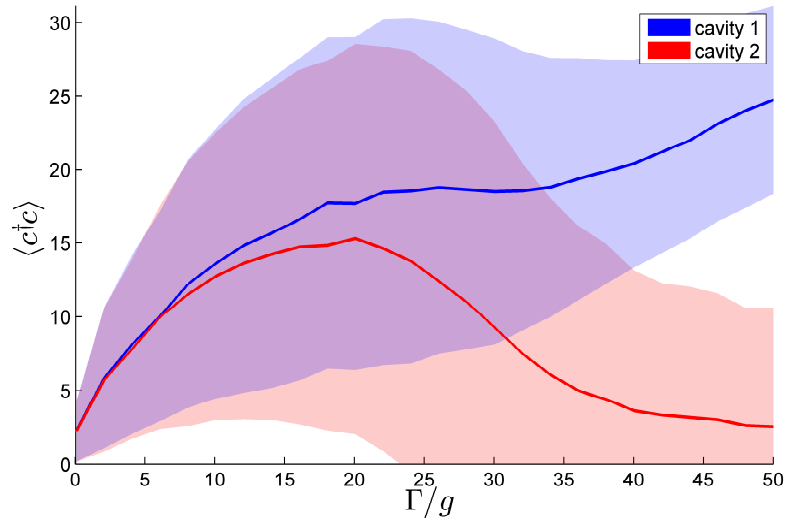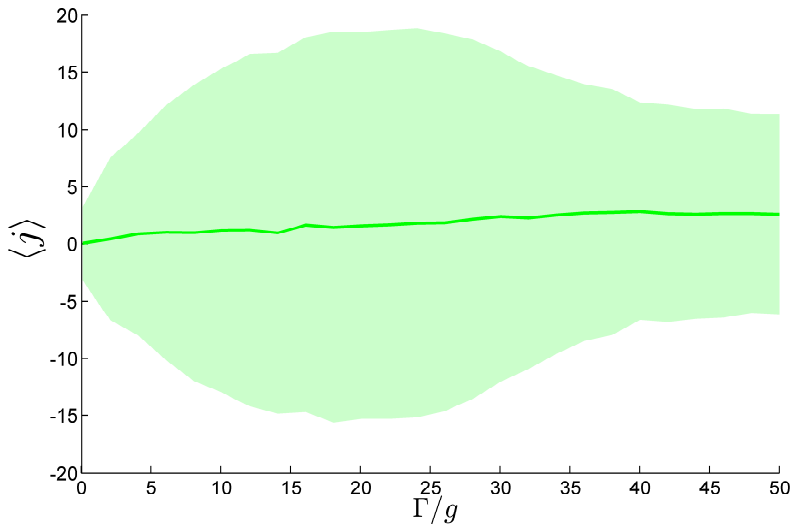
(a)
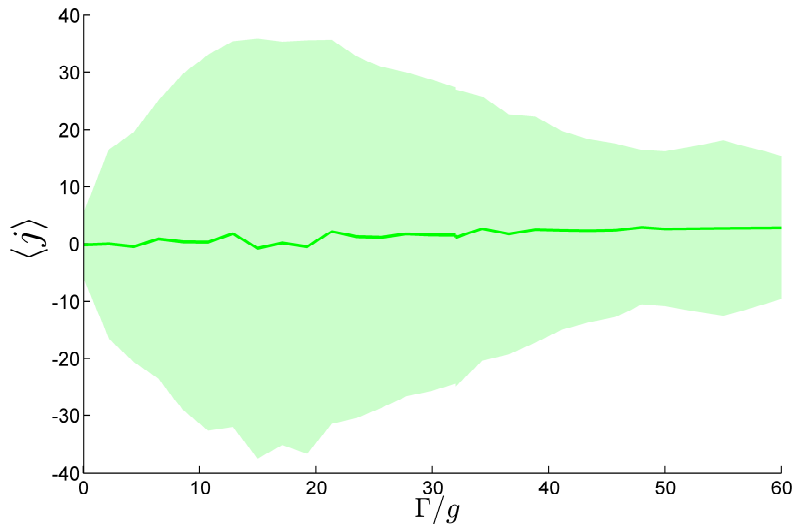
(b)

Figure 5.4: Quantum trajectory simulations with an overall damping $\kappa = 10^{-4}g$ in the quantum regime $(n_0 = 1)$ for $\nu = 2$. a) The mean steady state occupation number is plotted as a function Γ/g. For low Γ/g the cavities are on average equally distributed, the system is $\mathcal{PT}$-symmetric. For $\Gamma/g > 25$ the mean photon number differs in the two cavities and the $\mathcal{PT}$-symmetry is broken. In the symmetric regime, the variance of the occupation number grows with the occupation and reaches its maximum at the transition point. While in the symmetric regime the variance is quite large, for high Γ/g in the broken regime the variance is low and system resembles two nearly perfect coherent states. b) Mean current between the coupled gain and loss system. The fluctuations of the current increase for higher Γ/g until the transition point where it starts to decrease again. Each cavity consisted of 128 Fock states and 1000 trajectories were calculated and averaged.

(a)

(b)

Figure 5.5: Quantum trajectory simulations with an overall damping $\kappa = 10^{-3}g$ in the quantum regime $(n_0 = 1)$ for $\nu = 2$. a) The mean steady state occupation number is plotted as a function Γ/g. For low Γ/g the cavities are on average equally distributed, the system is $\mathcal{PT}$-symmetric. For $\Gamma/g > 8$ the mean photon number slightly differs and at $\Gamma/g = 22$ the states begin to completely differ and a phase transition occurs. In the symmetric regime, the variance of the occupation number grows with the occupation and reaches its maximum at the transition point. While in the symmetric regime the variance is quite large, for high Γ/g in the broken regime the variance is low and system resembles two nearly perfect coherent states. b) Mean current between the coupled gain and loss system. The fluctuations of the current increase for higher Γ/g until the transition point where it starts to decrease again. Each cavity consisted of 90 Fock states and 5000 trajectories were calculated and averaged.
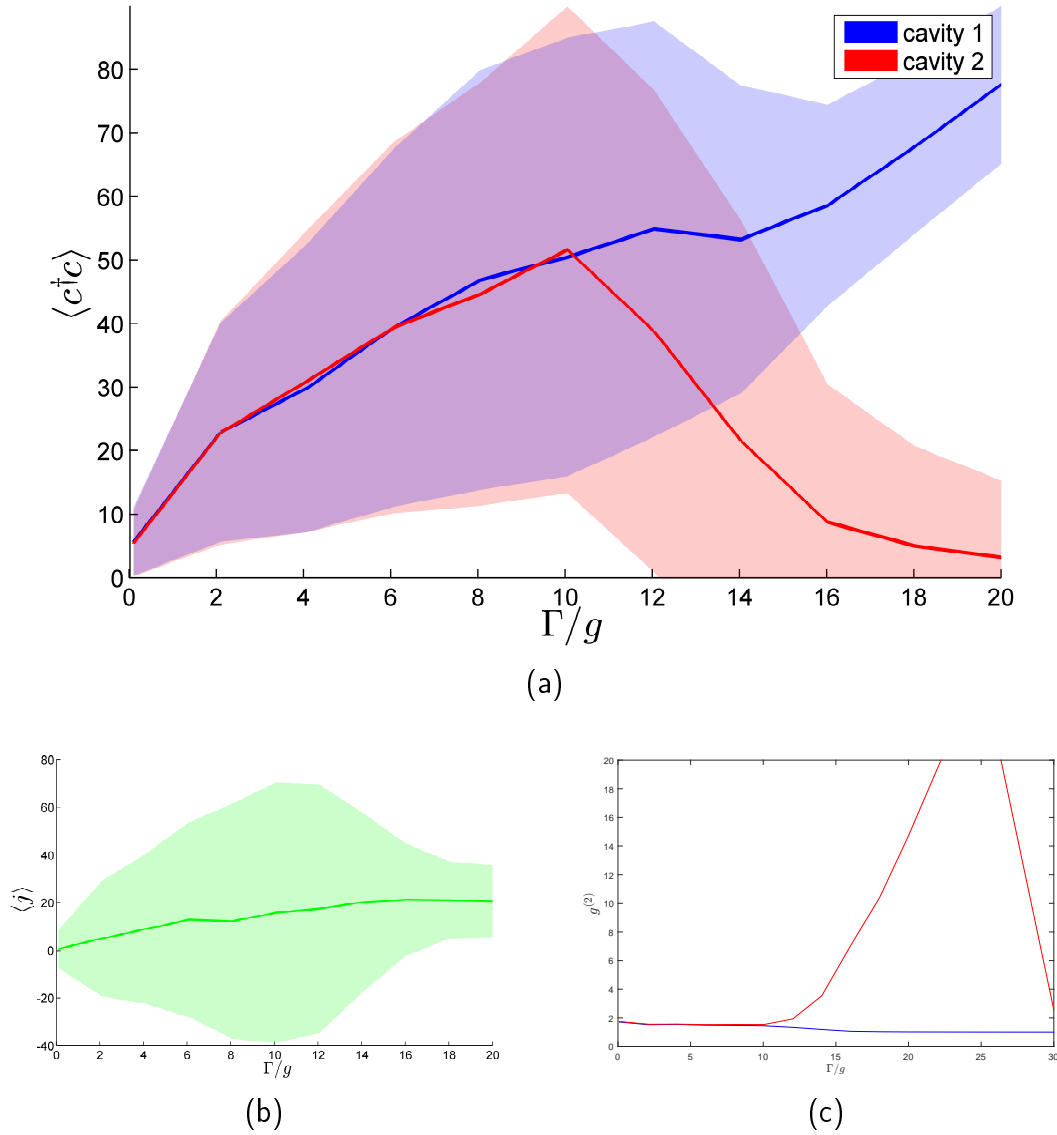
(a)

(b)

(c)

Figure 5.6: Quantum trajectory simulations with an overall damping $\kappa = 10^{-3}g$ in the quantum regime $(n_0 = 10)$ for $\nu = 2$ where each cavity consisted of 200 Fock states and 1000 trajectories were calculated and averaged. a) The mean steady state occupation number is plotted as a function Γ/g. For low Γ/g the cavities are on average equally distributed, the system is $\mathcal{PT}$-symmetric. For $\Gamma/g > 10$ the states begin to differ, a phase transition occurs. While in the symmetric regime the variance is quite large and reaches its maximum at the transition point, for high Γ/g in the broken regime the variance is again low and system resembles two nearly perfect coherent states.
b) Mean current between the coupled gain and loss system at different Γ/g. The fluctuations of the current increase for higher Γ/g until the symmetry breaking point. For higher Γ/g than the $\mathcal{PT}$-symmetry breaking point, the fluctuations get less until they reach a minimum, limited by uncertainty of coherent states. c) The second order correlation function $g^{(2)}$ is evaluated at different Γ/g. In the symmetric regime $g^{(2)} \approx 1.5$, which can be referred to as a very noisy coherent state. Around the breaking point, the $g^{(2)}$ of the cavity with loss reaches very high values, indicating a phase transition. At high Γ/g, $g^{(2)}$ approaches 1, confirming that the system consists of two coherent states in the broken regime.

system resembles two nearly perfect coherent states with little variance. The fluctuations of the current between the two systems increase for higher Γ/g until the symmetry breaking point. For higher Γ/g than the $\mathcal{PT}$-symmetry breaking point the fluctuations decrease.

For a stronger overall damping $\kappa = 10^{-3}g$ there is an additional region where only the occupation slightly differs until a phase transition occurs at a similar value of Γ/g (Figure 5.5).

In the (almost) classical regime with a saturation number of $n_0 = 10$ the system shows a very similar behavior as in the quantum regime (Figure 5.6). Again there is a $\mathcal{PT}$-symmetric region with lots of fluctuation and a $\mathcal{PT}$-broken regime where the system is described by two coherent states.

One major difference is that the transition point moves for a more classical regime to smaller Γ/g, and is at $\Gamma/g = 10$ for $n_0 = 10$. Moreover, the transition from the symmetric to the broken regime is a lot sharper.

Further evidence that a phase transition appears can be gained by looking at the second order correlation function

$$g^{(2)} = \frac{\langle c^\dagger c^\dagger cc \rangle}{\langle c^\dagger c \rangle^2}. \tag{5.25}$$

In the symmetric regime $g^{(2)} \approx 1.5$, which can be referred to state with an uncertainty between a coherent state and a thermal state. Around the breaking point the $g^{(2)}$ of the cavity with loss reaches very high values, indicating the phase transition. At high Γ/g the second order correlation function reaches $g^{(2)} \approx 1$, confirming that the system consists of two coherent states in the broken regime.

5.2 Stochastic differential equation

Although the quantum trajectories method is very powerful, the computational limits can be reached quite easily, especially in the classical case with high amplitudes (see Figure 5.3). Thus, a different method is needed to better understand the transition from the classical to the quantum case. Therefore, we derive a Fokker-Planck equation for our problem, convert it to a stochastic differential equation, which can be easily simulated on a computer.

By using the methods described in section 3.2 there exists no Fokker-Planck equation (section 3.3) for the master equation of two coupled oscillators with effective non-linear gain and loss operators as in Equation 5.6. Nevertheless, we can make a classical approximation:

$$f(n)|\alpha\rangle = \frac{1}{\left(1 + \frac{c^\dagger c}{n_0}\right)^\nu}|\alpha\rangle \approx \frac{1}{\left(1 + \frac{|\alpha|^2}{n_0}\right)^\nu}|\alpha\rangle \tag{5.26}$$

which holds true in the classical case where the uncertainty is minimal and equivalently we can write

$$\left\langle \frac{1}{(1 + \frac{c^\dagger c}{n_0})^\nu} \right\rangle = \frac{1}{(1 + \frac{\langle c^\dagger c \rangle}{n_0})^\nu}. \tag{5.27}$$

By using the methods derived in chapter 3 and the classical approximation we can convert the master equation (Equation 5.6) into a Fokker-Planck equation

$$\frac{\partial P(\alpha, \beta)}{\partial t} = \left[\frac{\partial}{\partial \alpha} \left(ig\beta + \left(\kappa - \frac{\frac{\Gamma}{2}}{(1 + \frac{|\alpha|^2}{n_0})^\nu} \right) \alpha \right) + \frac{\partial}{\partial \alpha^*} \left(-ig\beta^* + \left(\kappa - \frac{\frac{\Gamma}{2}}{(1 + \frac{|\alpha|^2}{n_0})^\nu} \right) \alpha^* \right) \right.$$

$$+ \frac{\partial}{\partial \beta} \left(ig\alpha + \left(\kappa + \frac{\frac{\Gamma}{2}}{(1 + \frac{|\beta|^2}{n_0})^\nu} \right) \beta \right) + \frac{\partial}{\partial \beta^*} \left(-ig\alpha^* + \left(\kappa + \frac{\frac{\Gamma}{2}}{(1 + \frac{|\beta|^2}{n_0})^\nu} \right) \beta^* \right)$$

$$+ \frac{\partial^2}{\partial \alpha \partial \alpha^*} \left(\frac{\Gamma}{(1 + \frac{|\alpha|^2}{n_0})^\nu} \right) P(\alpha, \beta). \tag{5.28}$$

Again an overall linear loss κ was added. As Fokker-Planck equations are hard to solve both analytically and numerically, we convert the Fokker-Planck equation into a stochastic Ito equation as explained in subsection 3.4.1. The Ito stochastic differential equations read

$$d\alpha = -ig\beta dt + \left(-\kappa + \frac{\frac{\Gamma}{2}}{(1 + \frac{|\alpha|^2}{n_0})^\nu} \right) \alpha dt + \frac{\sqrt{\frac{\Gamma}{2}}}{(1 + \frac{|\alpha|^2}{n_0})^{\nu/2}} dW \tag{5.29}$$

$$d\alpha^* = ig\beta^* dt + \left(-\kappa + \frac{\frac{\Gamma}{2}}{(1 + \frac{|\alpha|^2}{n_0})^\nu} \right) \alpha^* dt + \frac{\sqrt{\frac{\Gamma}{2}}}{(1 + \frac{|\alpha|^2}{n_0})^{\nu/2}} dW^* \tag{5.30}$$

$$d\beta = -ig\alpha dt + \left(-\kappa + \frac{\frac{\Gamma}{2}}{(1 + \frac{|\beta|^2}{n_0})^\nu} \right) \beta dt \tag{5.31}$$

$$d\beta^* = ig\alpha^* dt + \left(-\kappa + \frac{\frac{\Gamma}{2}}{(1 + \frac{|\beta|^2}{n_0})^\nu} \right) \beta^* dt \tag{5.32}$$

with $dW = (dW_1 + idW_2)$ where dW_i are Wiener increments.
Further insight can be gained by introducing polar coordinates $\alpha = \sqrt{n_0} r e^{i\phi_\alpha}$ and $\beta = \sqrt{n_0} z e^{i\phi_\beta}$. The differential equation can be transformed to polar coordinates by using the chain rule and Ito's calculus and $\mathcal{O}(\Delta t)$

$$dr = \frac{1}{2}\left(\frac{dr}{d\alpha}d\alpha + \frac{dr}{d\alpha^*}d\alpha^* + \frac{1}{2}\left(\frac{d^2r}{d\alpha^2}d\alpha^2 + \frac{d^2r}{d\alpha^{*2}}d\alpha^{*2} \right) \right), \tag{5.33}$$

$$dz = \frac{1}{2}\left(\frac{dr}{d\beta}d\beta + \frac{dr}{d\beta^*}d\beta^* + \frac{1}{2}\left(\frac{d^2r}{d\beta^2}d\beta^2 + \frac{d^2r}{d\beta^{*2}}d\beta^{*2} \right) \right), \tag{5.34}$$

$$d\phi_\alpha = \frac{1}{2}\left(\frac{d\phi_\alpha}{d\alpha}d\alpha + \frac{d\phi_\alpha}{d\alpha^*}d\alpha^* + \frac{1}{2}\left(\frac{d^2\phi_\alpha}{d\alpha^2}d\alpha^2 + \frac{d^2\phi_\alpha}{d\alpha^{*2}}d\alpha^{*2} \right) \right), \tag{5.35}$$

and

$$d\phi_\beta = \frac{1}{2}\left(\frac{d\phi_\beta}{d\beta}d\beta + \frac{d\phi_\beta}{d\beta^*}d\beta^* + \frac{1}{2}\left(\frac{d^2\phi_\beta}{d\beta^2}d\beta^2 + \frac{d^2\phi_\beta}{d\beta^{*2}}d\beta^{*2} \right) \right). \tag{5.36}$$

In polar coordinates the stochastic differential equations now read

$$dr = \left(\frac{\frac{\Gamma}{2}}{(1 + r^2)^\nu} - \kappa \right) rdt - gz\sin\phi dt + \frac{1}{\sqrt{n_0}}\sqrt{\frac{\Gamma}{2}}\frac{1}{(1 + r^2)^\nu}(\cos\phi_\alpha dW_1 + \sin\phi_\alpha dW_2), \tag{5.37}$$

$$dz = \left(-\frac{\frac{\Gamma}{2}}{(1 + z^2)^\nu} - \kappa \right) zdt + gr\sin\phi dt, \tag{5.38}$$

and

$$d\phi = d(\phi_\alpha - \phi_\beta) = g\left(\frac{r}{z} - \frac{z}{r}\right)\cos\phi dt + \frac{1}{\sqrt{n_0}}\sqrt{\frac{\Gamma}{2}}\frac{1}{r(1 + r^2)^{\nu/2}}(-\sin\phi_\alpha dW_1 + \cos\phi_\alpha dW_2), \tag{5.39}$$

where $\phi = \phi_\alpha - \phi_\beta$. From the equations of motion for r, we can clarify the meaning of the photon saturation number. The smaller n_0, the more quantum noise exists.

For a very large n_0 the stochastic term can be neglected and the equations coincide with the classical equations with no noise.

We now focus on the steady state solutions in the classical case with no noise and will later investigate the differences when noise is present.

5.2.1 Classical analysis

In the classical case (no diffusion $dW = 0$) we obtain the following equations in steady state:

$$\frac{dr}{dt} = \left(\frac{\frac{\Gamma}{2}}{(1 + r^2)^\nu} - \kappa \right) r - gz \sin \phi = 0 \tag{5.40}$$

$$\frac{dz}{dt} = \left(-\frac{\frac{\Gamma}{2}}{(1 + z^2)^\nu} - \kappa \right) z + gr \sin \phi = 0 \tag{5.41}$$

$$\frac{d\phi}{dt} = g(\frac{r}{z} - \frac{z}{r}) \cos \phi = 0 \tag{5.42}$$

From the last equation it directly follows that $\phi_{ss} = \pm \frac{\pi}{2}$ in steady state. Due to finite κ, the stationary occupation number of the gain mode $|\alpha|^2$ is always slightly larger than that of the loss mode $|\beta|^2$, therefore $\phi = \frac{\pi}{2}$ is the stable solution.

By setting $\phi = \frac{\pi}{2}$ and $\tilde{\Gamma}(r) = \frac{\frac{\Gamma}{2}}{(1+r^2)^\nu}$ we arrive at the following set of equations

$$\frac{dr}{dt} = (\tilde{\Gamma}(r) - \kappa)r - gz = 0, \tag{5.43}$$

$$\frac{dz}{dt} = (-\tilde{\Gamma}(z) - \kappa)z + gr = 0. \tag{5.44}$$

For a detailed analysis of the steady state solution we use the trace-determinant plane of the Jacobian, where the non-linear system is linearized near an equilibrium point. The Jacobian for our system reads

$$J = \begin{pmatrix} \tilde{\Gamma}'(r)r + \tilde{\Gamma}(r) - \kappa & -g \\ g & -\tilde{\Gamma}'(z)z - \tilde{\Gamma}(r) - \kappa \end{pmatrix} \tag{5.45}$$

where the primes denotes the spatial derivative. The trace and determinant of J are

$$\tau = \text{Tr}(J) = \Gamma'(r)r + \tilde{\Gamma}(r) - \Gamma'(z)z - \tilde{\Gamma}(r) - \kappa \tag{5.46}$$

and

$$\Delta = \det(J) = (\tilde{\Gamma}'(r)r + \tilde{\Gamma}(r) - \kappa)(-\tilde{\Gamma}'(z)z - \tilde{\Gamma}(r) - \kappa) + g^2. \tag{5.47}$$
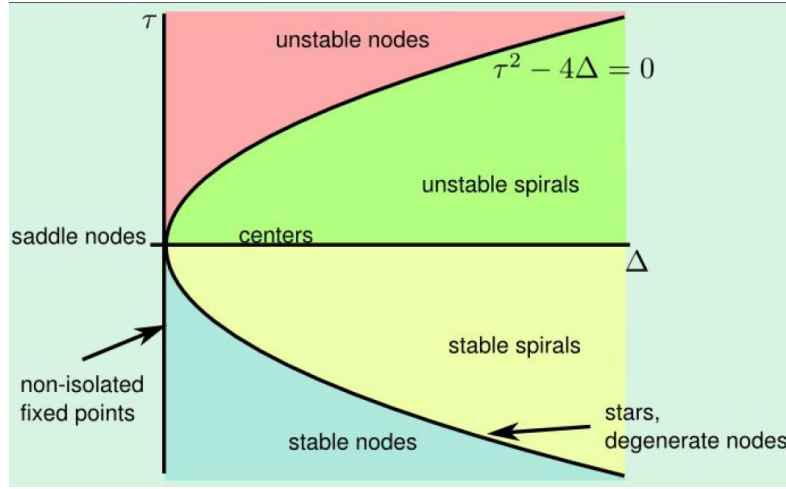
Figure 5.7: Classification of a fixed point according to the trace (τ) and determinant (Δ) of the Jacobian J. Taken from [20].

For a 2-dimensional system the eigenvalues $\lambda_{1,2}$ can be written in terms of τ and Δ:

$$\lambda_1 = \frac{\tau + \sqrt{\tau^2 - 4\Delta}}{2} \tag{5.48}$$

$$\lambda_2 = \frac{\tau - \sqrt{\tau^2 - 4\Delta}}{2}. \tag{5.49}$$

Moreover, $\Delta = \lambda_1\lambda_2$ and $\tau = \lambda_1 + \lambda_2$. Thus if $\Delta < 0$ then the eigenvalues are of opposite sign, and the fixed point is a saddle. For $\Delta > 0$ both eigenvalues have the same sign and for $\tau > 0$ both are positive and the point is unstable while for $\tau < 0$ both eigenvalues are negative and stable. The discriminant $\sqrt{\tau^2 - 4\Delta}$ denotes if the point is nodal or spiral (i.e. if the eigenvalues are real or complex). Figure 5.7 illustrates the different stability region in the trace-determinant plane of the Jacobian. As a next step, we use this method to investigate the stability of the solutions for the steady state equations (Equation 5.43 and Equation 5.44) and define phases (parameter regime of Γ/g) where a solution is stable [9].

Phase I:

For Equation 5.43 and Equation 5.44 there exists the trivial solution

$$r_{ss} = z_{ss} = 0. \tag{5.50}$$

By inserting Equation 5.50 into Equation 5.46 and Equation 5.47 we get

$$\tau = -2\kappa \tag{5.51}$$

and
$$\Delta = g^2 - \left(\frac{\Gamma}{2}\right)^2 + \kappa^2. \tag{5.52}$$

We can conclude that Equation 5.50 corresponds to a stable spiral for $\frac{\Gamma}{2} < g$ and a stable saddle node for $\frac{\Gamma}{2} > g$. We thus conclude that phase I is exhibited for

$$0 < \frac{\Gamma}{2g} < 1. \tag{5.53}$$

Phase II:

We assume that the occupation numbers are nearly equal, however simply assuming $r_{ss} = z_{ss}$ yields an inconsistency due to a finite κ. Therefore we expand r_{ss} and z_{ss} in orders of κ: $r_{ss} = r_{ss}^0 + \kappa r_{ss}^1 + ...$ and $z_{ss} = z_{ss}^0 + \kappa z_{ss}^1 + ...$. We get

$$r_{ss}^{(0)} = z_{ss}^{(0)} = \sqrt{-1 + \left(\frac{\Gamma}{2g}\right)^{1/\nu}} \tag{5.54}$$

and
$$r_{ss}^{(1)} = -z_{ss}^{(1)} = r_{ss}^{(0)}[\tilde{\Gamma}'(r_{ss}^{(0)})r_{ss}^{(0)} + \tilde{\Gamma}(r_{ss}^{(0)}) + g]^{-1}. \tag{5.55}$$

The Jacobian trace reads

$$\begin{aligned}
\tau &= -2\kappa \left(1 - \frac{\tilde{\Gamma}''(r_{ss}^{(0)})r_{ss}^{(0)2} + 2\tilde{\Gamma}'(r_{ss}^{(0)})}{\tilde{\Gamma}'(r_{ss}^{(0)})r_{ss}^{(0)} + \tilde{\Gamma}(r_{ss}^{(0)}) + g}\right) \\
&= -2\kappa \left(1 - \frac{2\nu[(\Gamma/(2g))^{1/\nu} - 1][(2\nu - 1)(\Gamma/(2g))^{1/\nu} - 2(\nu + 1)]}{2\nu(\Gamma/(2g))^{1/\nu} + 2(1 - \nu)(\Gamma/(2g))^{2/\nu}}\right)
\end{aligned} \tag{5.56}$$

and the determinant

$$\Delta = g^2 - [\tilde{\Gamma}'(r_{ss}^{(0)})r_{ss}^{(0)} + \tilde{\Gamma}(r_{ss}^{(0)})]^2 = g^2 - g^2[2\nu - 1 - 2\nu(\Gamma/(2g))^{-1/\nu}]^2. \tag{5.57}$$

We see that $\Delta > 0$ for $2 < 2\Gamma/g < [\nu/(\nu - 1)]^\nu$. Moreover, $\tau < 0$ for $\Gamma/g < 2[(\nu + 2\nu^2 + \sqrt{2\nu + 3\nu^2})/(2\nu^2 - 1)]^\nu$.

We thus conclude that phase II is exhibited for

$$2 < \frac{\Gamma}{g} < \min\left\{2\left(\frac{\nu + 2\nu^2 + \sqrt{2\nu + 3\nu^2}}{2\nu^2 - 1}\right)^\nu, 2\left(\frac{\nu}{\nu - 1}\right)^\nu\right\}. \tag{5.58}$$

We find for $1 \le \nu < 2$

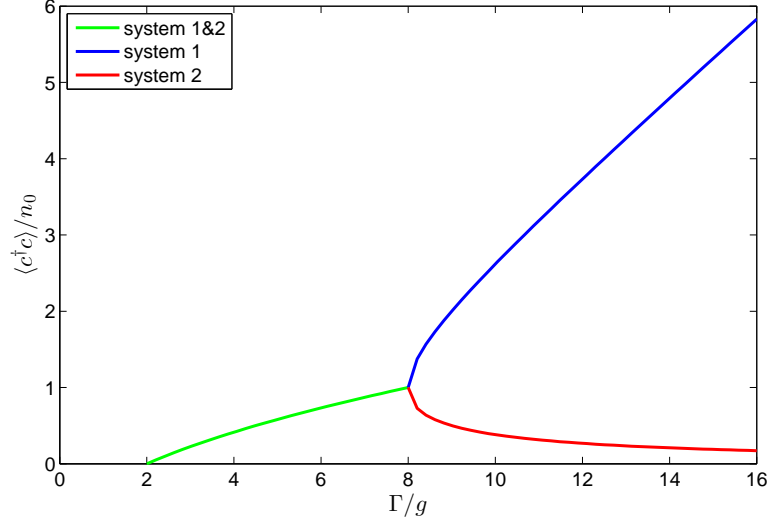$$2 < \frac{\Gamma}{g} < 2\left(\frac{\nu + 2\nu^2 + \sqrt{2\nu + 3\nu^2}}{2\nu^2 - 1}\right)^\nu \tag{5.59}$$

Figure 5.8: The classical solution of two coupled phonon lasers ($\nu = 2$) where one experiences non-linear gain and the other non-linear loss as a function of $\frac{\Gamma}{g}$, the ratio between gain/loss to the coupling strength. In the absence of noise, both systems are not populated at all for $\frac{\Gamma}{g} < 2$. For $2 < \frac{\Gamma}{g} < 8$ the system is $\mathcal{PT}$-symmetric where both systems are equally populated. At $\frac{\Gamma}{g} = 8$ this symmetry suddenly breaks and for higher $\frac{\Gamma}{g}$ system 1 is significantly higher populated than system 2.

and for $\nu \geq 2$

$$2 < \frac{\Gamma}{g} < 2 \left(\frac{\nu}{\nu - 1} \right)^{\nu}. \tag{5.60}$$

Phase III

We distinguish between the case of a conventional laser with $\nu = 1$ and a phonon laser with $\nu = 2$.

In the case of $\nu = 1$ and $\Gamma/g > 2[(\nu + 2\nu^2 + \sqrt{2\nu + 3\nu^2})/(2\nu^2 - 1)]^{\nu}$ two amplitudes undergo limit cycles. This phase can be referred to as weakly broken phase. For a detailed analysis see [9].

For the case of $\nu = 2$ we get

$$r_{ss}^2 = \frac{\frac{\Gamma}{2} + \sqrt{\frac{\Gamma^2}{4} - 2\Gamma g}}{2g} - 1, \tag{5.61}$$

$$z_{ss}^2 = \frac{\frac{\Gamma}{2} - \sqrt{\frac{\Gamma^2}{4} - 2\Gamma g}}{2g} - 1, \tag{5.62}$$

which corresponds to a stable spiral while

$$r_{ss}^2 = \frac{\frac{\Gamma}{2} - \sqrt{\frac{\Gamma^2}{4} - 2\Gamma g}}{2g} - 1, \tag{5.63}$$

$$z_{ss}^2 = \frac{\frac{\Gamma}{2} + \sqrt{\frac{\Gamma^2}{4} - 2\Gamma g}}{2g} - 1, \tag{5.64}$$

corresponds to an unstable spiral. As $r_{ss}^2 > z_{ss}^2$ the system is not $\mathcal{PT}$-symmetric any more. We can conclude that in the classical case for $\nu = 1$ there is no symmetry breaking while for $\nu = 2$ the $\mathcal{PT}$-symmetry is broken at $\Gamma/g = 8$.

5.2.2 Results of simulations

First we focus on the case of two coupled optical laser ($\nu = 1$), where we can extend our analysis to really large values of Γ/g. Results of numerical simulations of the stochastic differential Ito equations in the classical regime ($n_0 = 10$) show that for low Γ/g the populations of the system coincide while for really high Γ/g the occupations of the two systems differ (see Figure 5.9). Nevertheless, the variance of the population stays proportional to the population in both regions. Moreover, there is no difference in the current between the region where the occupation is the same and where it differs. These results confirm our assumption that the phase transition observed by the quantum trajectories method (see Figure 5.3) at high Γ/g is only due to the consideration of a small number of Fock states. Again we can conclude that the symmetry is only weakly broken. Simulations in the quantum regime ($n_0 = 1$) reveal no significantly different results. The classical equations show that the systems undergo limit cycles while the simulation with noise reveal that these oscillations are washed out by the noise.

Numerical simulations of the stochastic differential Ito equations of a phonon laser ($\nu = 2$) in the classical regime ($n_0 = 10$) show $\mathcal{PT}$-symmetry breaking (see Figure 5.10). For low Γ/g the mean occupation and the fluctuations are identical for both systems. At $\Gamma/g \approx 14$ this symmetry suddenly breaks and the population differs. Moreover, there is a sudden drop of fluctuations. In addition, the fluctuation of the current suddenly drop as well. In the broken regime the mean current is constant.

Further insight can be gained by evaluating the second order correlation function $g^{(2)}$ at different Γ/g. While in the symmetric regime $g^{(2)} \approx 1.4$, which refers to a noisy state with an uncertainty between a coherent and a thermal state. Around the breaking point $\Gamma/g \approx 14$, $g^{(2)}$ reaches very high values, confirming a phase transition. For high Γ/g in the broken regime $g^{(2)} = 1$, the system resembles two coherent states.
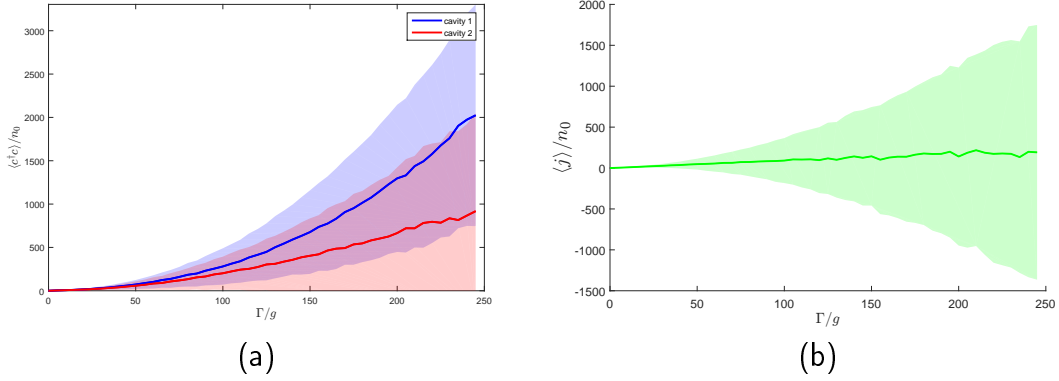
(a)   (b)

Figure 5.9: Results of numerical simulations of the stochastic differential Ito equations for coupled optical laser ($nu = 1$) in the classical regime ($n_0 = 10$) and an overall loss $\kappa = 10^{-2}g$. (a) The occupation as a function of Γ/g is plotted. For really high Γ/g the occupation of the two systems differ, nevertheless its variances stay proportional. (b) The current as a function of Γ/g is plotted. We cannot find any difference between the region where the occupation is the same and where it differs. We therefore conclude that the symmetry is only weakly broken.

The classical calculations without noise show that the phase between the two harmonic oscillators is fixed at $\phi = \frac{\pi}{2}$. This holds true only in the $\mathcal{PT}$-broken regime in the presence of quantum noise (Figure 5.11). Moreover, in the symmetric regime ϕ follows a broad distribution while in the broken regime there is almost no uncertainty. As a consequence, the expectation of $\langle \sin(\phi) \rangle$ which is proportional to the current is 0.1 in the symmetric regime and 1 in the broken regime. From this we can conclude that in the $\mathcal{PT}$-symmetric regime, energy is often exchanged back and forth resulting in a low net current while in the broken regime energy is efficiently transferred in one direction from the oscillator which experiences non-linear gain to the other one which experience non-linear loss.

To clarify the difference between the two regimes we investigate the steady state distributions of the trajectories in the complex plane (see Figure 5.12). In the symmetric region the steady state distributions form a very broad ring in the complex plane. Moreover, the distributions of the two systems do not differ. In the broken regime, the distribution is very narrow and both systems are clearly separated.

Comparison with the classical calculation without noise (Figure 5.8) shows that the major difference in the symmetric regime is that the system is populated even for $\Gamma/g < 2$. Moreover, the system is more highly populated with lots of noise in contrast to the classical calculation. Nevertheless, the results coincide in the symmetry broken regime. In contrast to the purely classical calculation the $\mathcal{PT}$-symmetry breaking point is at $\Gamma/g \approx 14$ instead of $\Gamma/g = 8$.
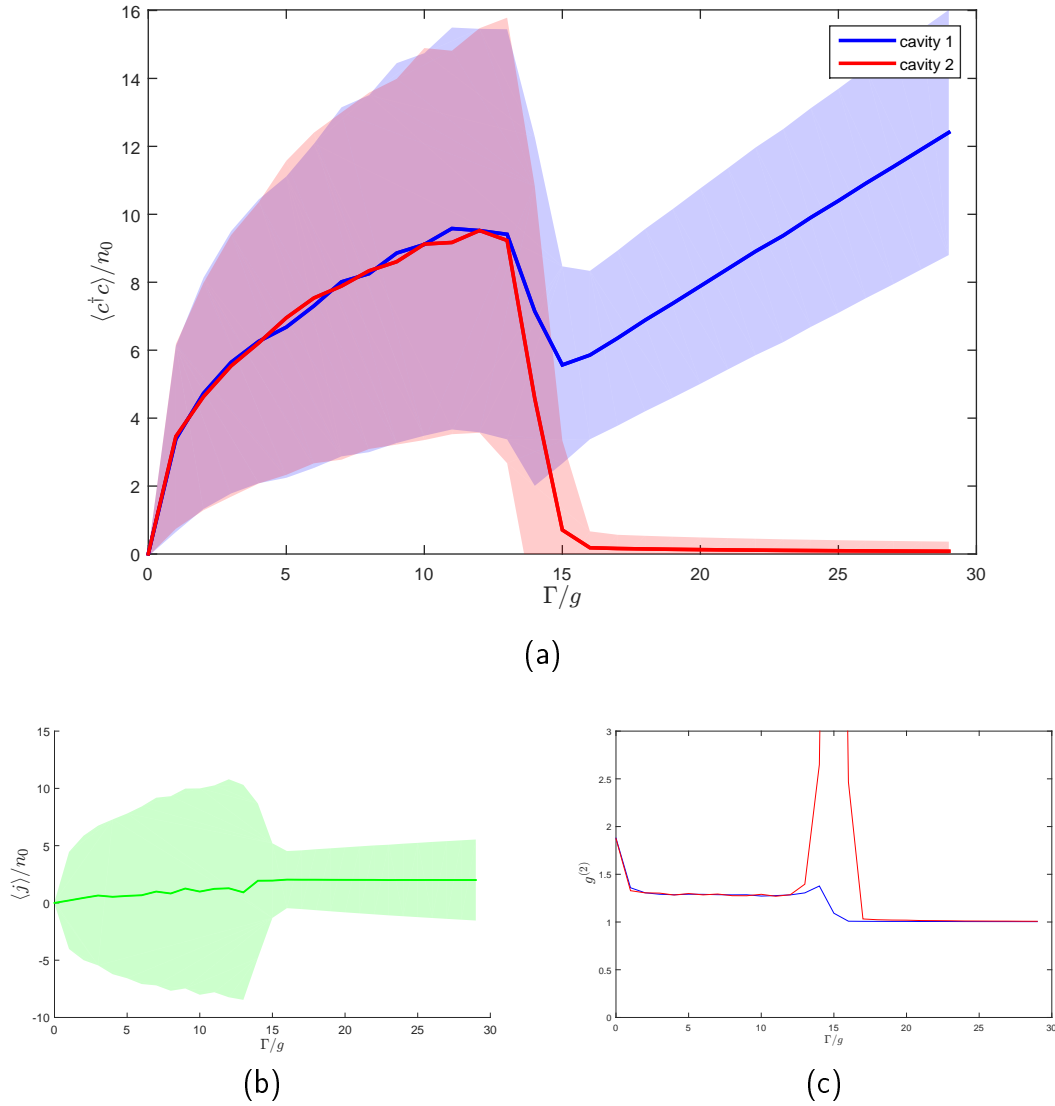
(a)

(b)

(c)

Figure 5.10: Results of numerical simulations of the stochastic differential Ito equations for coupled phonon laser ($\nu = 2$) in the classical regime ($n_0 = 10$) and an overall loss $\kappa = 10^{-3}g$. Around 2000 trajectories where calculated and averaged to obtain this result. (a) Mean occupation as a function of Γ/g. For low Γ/g the mean occupation and the fluctuations are in both systems the same. At $\Gamma/g \approx 14$ this symmetry suddenly breaks and the population differs. Moreover there is a sudden drop of fluctuations. In addition, the fluctuation of the current suddenly drop too (b). In the broken regime the mean current is constant. (c) The second order correlation function $g^{(2)}$ at different Γ/g. While in the symmetric regime $g^{(2)} \approx 1.4$, which refers to a noisy coherent state, the $g^{(2)}$ reaches very high values around the breaking point $\Gamma/g = 14$, verifying a phase transition. For high Γ/g in the broken regime $g^{(2)} = 1$, resembling coherent states.

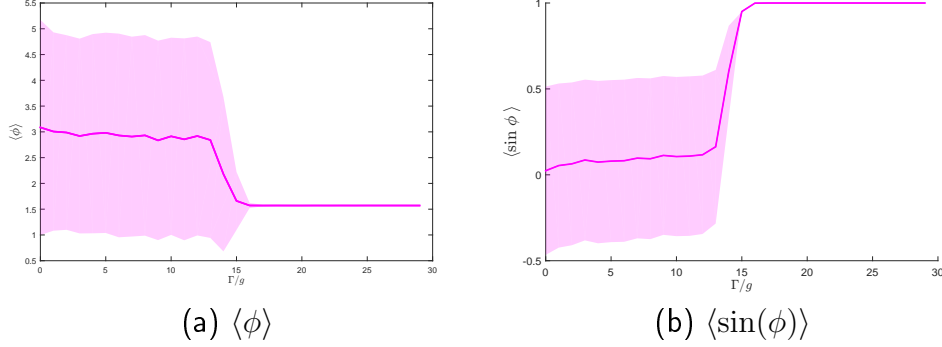(a) $\langle \phi \rangle$ (b) $\langle \sin(\phi) \rangle$

Figure 5.11: Steady state solution of (a) $\langle \phi \rangle$ and (b) $\langle \sin(\phi) \rangle$ for a phonon laser ($\nu = 2$) with a phonon saturation number of $n_0 = 10$ at different Γ/g, where $\phi = \arg(\alpha) - \arg(\beta)$. While in the low Γ/g regime where the system is $\mathcal{PT}$-symmetric the phase between the oscillators is widely distributed with an average of $\langle \phi \rangle = \pi$ and the sine of the phase which is proportional to the current is $\langle \sin(\phi) \rangle = 0.1$, the phase is fixed $\langle \phi \rangle = \frac{\pi}{2}$ and $\langle \sin(\phi) \rangle = 1$ in the broken regime. Results were observed by stochastic differential equations simulations with 2000 trajectories with an overall loss $\kappa = 10^{-3}g$.
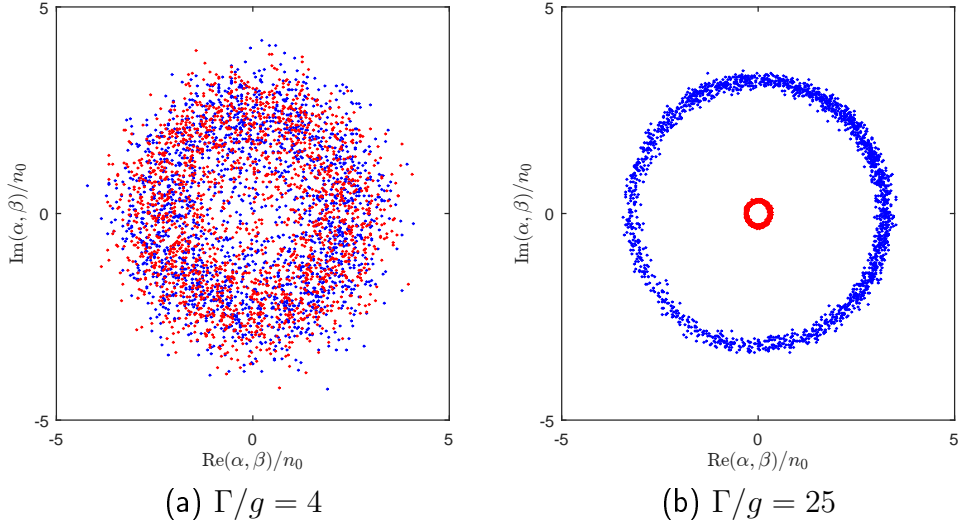

(a) $\Gamma/g = 4$ (b) $\Gamma/g = 25$

Figure 5.12: Steady state distributions of stochastic differential equations simulations of a phonon laser ($\nu = 2$) with a phonon saturation number of $n_0 = 10$ and an overall loss $\kappa = 10^{-3}$. While in the $\mathcal{PT}$-symmetric regime ($\Gamma/g = 4$) the steady state distribution form a very broad ring in the complex plane and the two systems are not distinguishable, the distribution is very narrow and the both systems are clearly separated.
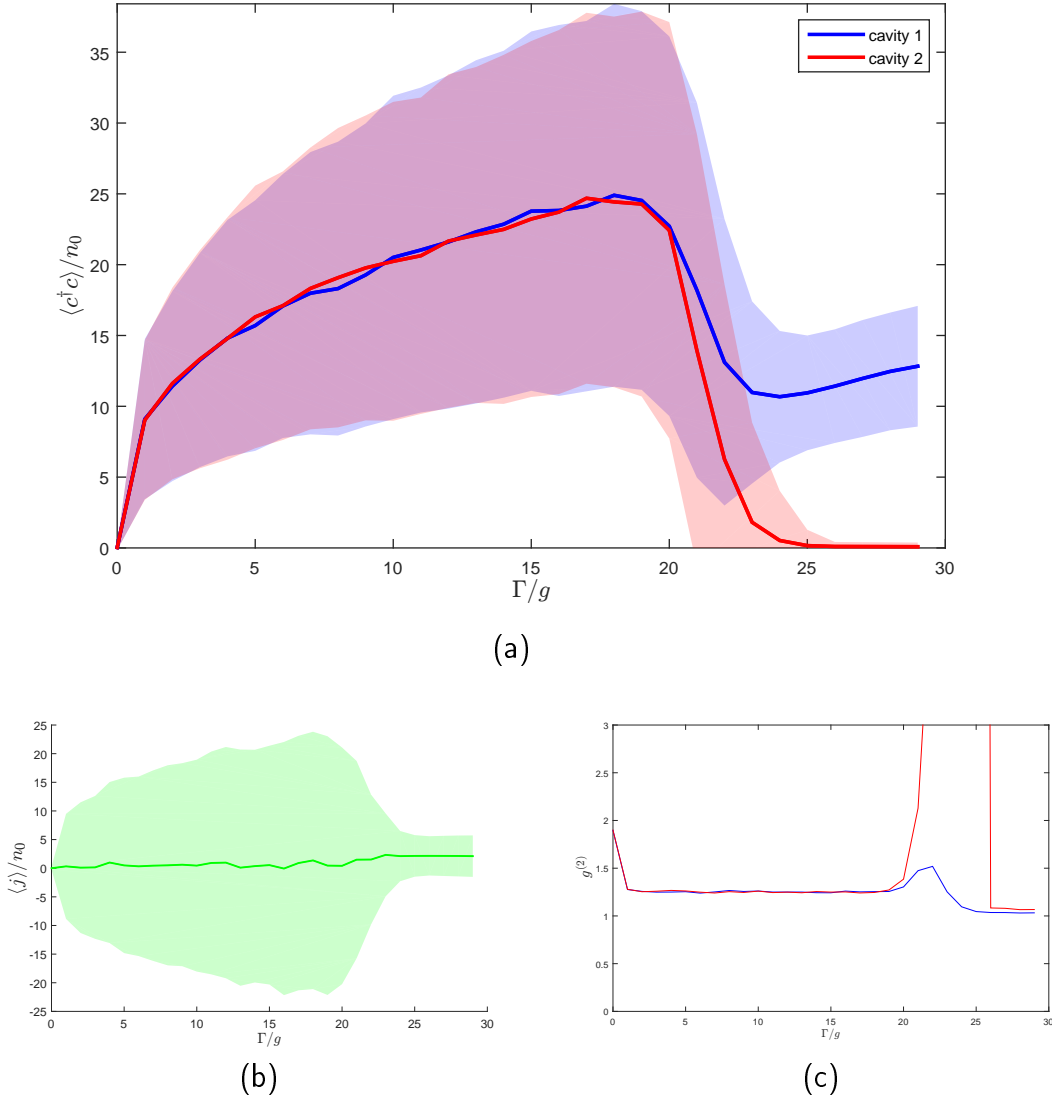
(a)

(b)

(c)

Figure 5.13: Results of numerical simulations of the stochastic differential Ito equations for coupled phonon lasers ($\nu = 2$) in the quantum regime ($n_0 = 10$) and an overall loss $\kappa = 10^{-3}g$. Around 2000 trajectories where calculated and averaged to obtain this result. (a) Mean occupation as a function of Γ/g. For low Γ/g the mean occupation and the fluctuations are in both systems the same. At $\Gamma/g \approx 22$ this symmetry suddenly breaks and the population differs. Moreover there is a sudden drop of fluctuations. (b) The mean current in the $\mathcal{PT}$-symmetric regime is governed by large fluctuations. For Γ/g larger than the breaking points the fluctuation significantly drops and the mean current is constant for different Γ/g. (c) The second order correlation function $g^{(2)}$ at different Γ/g. While in the symmetric regime $g^{(2)} \approx 1.3$, which refers to a noisy coherent state, the $g^{(2)}$ diverges around the breaking point at $\Gamma/g \approx 22$, verifying a phase transition. For higher Γ/g the second order correlation function is $g^{(2)} \approx 1$, resembling coherent states.
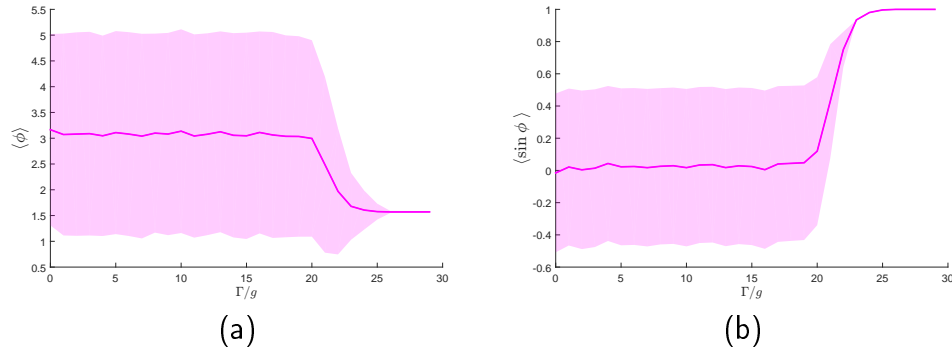
(a)   (b)

Figure 5.14: Steady state solution of (a) $\langle\phi\rangle$ and (b) $\langle\sin(\phi)\rangle$ for a phonon laser ($\nu = 2$) with a phonon saturation number of $n_0 = 1$ (quantum regime) at different Γ/g, where $\phi = \arg(\alpha) - \arg(\beta)$. While in the low Γ/g regime where the system is $\mathcal{PT}$-symmetric the phase between the oscillators is widely distributed with an average of $\langle\phi\rangle = \pi$ and the sine of the phase which is proportional to the current is $\langle\sin(\phi)\rangle = 0.1$, the phase is fixed $\langle\phi\rangle = \frac{\pi}{2}$ and $\langle\sin(\phi)\rangle = 1$ in the broken regime. Results were observed by stochastic differential equations simulations with 2000 trajectories with an overall loss $\kappa = 10^{-3}g$.
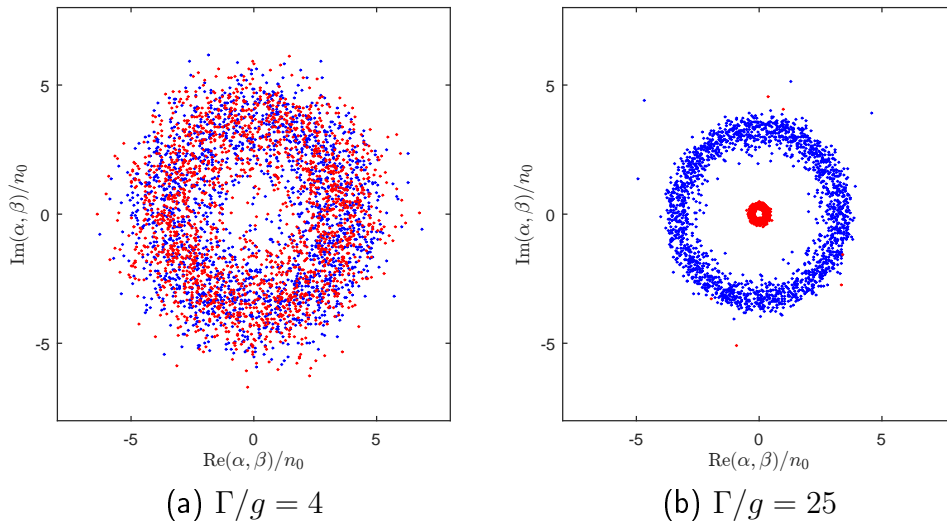

(a) $\Gamma/g = 4$ (b) $\Gamma/g = 25$

Figure 5.15: Steady state distributions of stochastic differential equations simulations of a phonon laser ($\nu = 2$) with a phonon saturation number of $n_0 = 1$ and an overall loss $\kappa = 10^{-3}$. While in the $\mathcal{PT}$-symmetric regime ($\Gamma/g = 4$) the steady state distribution form a very broad ring in the complex plane and the two systems are not distinguishable, the distribution is narrower and the both systems are clearly separated.

To better understand the behavior in the symmetric regime, we calculate the expectation values of the quadratic operators. Therefore we substitute $\alpha \to \sqrt{n_0}\alpha$, $\beta \to \sqrt{n_0}\beta$ and get the following equations for the expectation values:

$$\frac{d\left\langle |\alpha|^2 \right\rangle}{dt} = ig\left\langle \alpha\beta^* \right\rangle - ig\left\langle \alpha^*\beta \right\rangle + \left\langle (-2\kappa + \frac{\Gamma}{(1+|\alpha|^2)^\nu})|\alpha|^2 \right\rangle + \frac{1}{n_0}\left\langle \frac{\Gamma}{(1+|\alpha|^2)^\nu} \right\rangle,$$ (5.65)

$$\frac{d\left\langle |\beta|^2 \right\rangle}{dt} = -ig\left\langle \alpha\beta^* \right\rangle + ig\left\langle \alpha^*\beta \right\rangle + \left\langle (-2\kappa - \frac{\Gamma}{(1+|\beta|^2)^\nu})|\beta|^2 \right\rangle,$$ (5.66)

$$\frac{d\left\langle |\alpha|^2 + |\beta|^2 \right\rangle}{dt} = -2\kappa\left\langle |\alpha|^2 + |\beta|^2 \right\rangle + \Gamma(\left\langle \frac{|\alpha|^2 + \frac{1}{n_0}}{(1+|\alpha|^2)^\nu} \right\rangle - \left\langle \frac{|\beta|^2}{(1+|\beta|^2)^\nu} \right\rangle).$$ (5.67)

We assume that in steady state the amplitudes of both systems coincide $|\alpha|^2 \approx |\beta|^2$ in the $\mathcal{PT}$-symmetric regime and get

$$\frac{d\left\langle |\alpha|^2 + |\beta|^2 \right\rangle}{dt} = -4\kappa\left\langle |\alpha|^2 \right\rangle + \frac{\Gamma}{n_0}\left\langle \frac{1}{(1+|\alpha|^2)^2} \right\rangle = 0.$$ (5.68)

As a result we can conclude for large $|\alpha|^2$, that the occupation number $|\alpha|^2$ behaves as the cubic root of $\frac{\Gamma}{g}$

$$|\alpha|^2 \approx \sqrt[3]{\frac{\Gamma}{4\kappa n_0}}.$$ (5.69)

This is in good agreement with the simulations and shows that the behavior in the symmetric regime is governed by the overall loss κ and by the saturation number n_0. The smaller the overall loss κ, the higher the population of a system in the symmetric regime. In addition, the more quantum a system is the higher is $\left\langle c^\dagger c \right\rangle /n_0$.

This can be confirmed by looking at the results of the simulation in the quantum regime with $n_0 = 1$ (Figure 5.13), where the mean occupation for Γ/g in the symmetric regime is around twice as large than for $n_0 = 10$. Again, in the symmetric regime the system can be described with two noisy states and in broken regime with two coherent states. This can also be reflected by looking at the phase space of the steady state solution (Figure 5.12). As well as for $n_0 = 10$, the mean value of occupation coincides with the classical solution (Equation 5.61 and Equation 5.62).

As opposed to $n_0 = 10$ the symmetry breaking point is at $\Gamma/g \approx 22$. We can conclude that the more quantum a system is, the more the breaking point moves towards higher Γ/g.

The phase between the two coupled oscillators shows similar behavior in the quantum regime (Figure 5.11) as in the classical regime. For $n_0 = 1$, $\langle \sin(\phi) \rangle$ equals 1 in the broken regime, but $\langle \sin(\phi) \rangle$ equals 0.05 instead of 0.1 in the symmetric regime.

5.2.3 Noise activation

Our analysis showed that the $\mathcal{PT}$-symmetry breaking point is at $\Gamma/g = 8$ in the purely classical case without any noise, at $\Gamma/g \approx 14$ for $n_0 = 10$ and $\Gamma/g \approx 22$ for $n_0 = 1$. In order to find an explanation for the shift of the breaking point to higher Γ/g, we linearize the differential equations with noise around the purely classical solution in the $\mathcal{PT}$-symmetry broken regime in order to find an expression of an effective noise for the second oscillator with non-linear loss.

By using the fact that the relative phase $\phi = \frac{\pi}{2}$ is constant in the whole regime even for different saturation numbers, the differential equations of the system in polar coordinates read

$$\frac{dr}{dt} = \left(\frac{\frac{\Gamma}{2}}{(1+r^2)^2} - \kappa \right) r - gz + \frac{1}{\sqrt{n_0}} \sqrt{\frac{\Gamma}{2}} \frac{1}{(1+r^2)} \xi(t), \qquad (5.70)$$

$$\frac{dz}{dt} = \left(-\frac{\frac{\Gamma}{2}}{(1+z^2)^2} - \kappa \right) z + gr. \qquad (5.71)$$

As a next step, we linearize these equations at the steady state solution. With $r = r_{ss} + \delta r$ and $z = z_{ss} + \delta z$ we arrive at

$$\frac{d(r_{ss} + \delta r)}{dt} = \left(\frac{\frac{\Gamma}{2}}{(1+r_{ss}^2)^2} - \kappa \right) r_{ss} + \frac{\partial}{\partial r} \left(\left(\frac{\frac{\Gamma}{2}}{(1+r^2)^2} - \kappa \right) r \right)_{r=r_{ss}} \delta r$$
$$- g(z_{ss} + \delta z) + \frac{1}{\sqrt{n_0}} \sqrt{\frac{\Gamma}{2}} \left(\frac{1}{(1+r_{ss}^2)} + \left(\frac{\partial}{\partial r} \frac{1}{(1+r^2)} \right)_{r=r_{ss}} \delta r \right) \xi(t), \qquad (5.72)$$

$$\frac{d(z_{ss} + \delta z)}{dt} = \left(-\frac{\frac{\Gamma}{2}}{(1+z_{ss}^2)^2} - \kappa \right) z_{ss} + \frac{\partial}{\partial z} (-\frac{\frac{\Gamma}{2}}{(1+z^2)^2} - \kappa)_{z=z_{ss}} \delta z + g(r_{ss} + \delta r). \qquad (5.73)$$

After inserting the steady state solutions, the equations reduce to differential equations of δr and δz

$$\dot{\delta r} = \frac{\partial}{\partial r} \left(\left(\frac{\frac{\Gamma}{2}}{(1+r^2)^2} - \kappa \right) r \right)_{r=r_{ss}} \delta r - g\delta z +$$
$$\frac{1}{\sqrt{n_0}} \sqrt{\frac{\Gamma}{2}} \left(\frac{1}{(1+r_{ss}^2)} + \left(\frac{\partial}{\partial r} \frac{1}{(1+r^2)} \right)_{r=r_{ss}} \delta r \right) \xi(t), \qquad (5.74)$$

$$\dot{\delta z} = \frac{\partial}{\partial z}\left(-\frac{\frac{\Gamma}{2}}{(1+z^2)^2} - \kappa\right)_{z=z_{ss}}\delta z + g\delta r, \tag{5.75}$$

where we neglected one term, because we assume that it is small. By introducing new variables $\tilde{\Gamma}(r_{ss}) = \frac{\partial}{\partial r}\left(\left(\frac{\frac{\Gamma}{2}}{(1+r^2)^2} - \kappa\right)r\right)_{r=r_{ss}}$, $\tilde{\Gamma}(z_{ss}) = \frac{\partial}{\partial z}\left(-\frac{\frac{\Gamma}{2}}{(1+z^2)^2} - \kappa\right)_{z=z_{ss}}$ and $D(r_{ss}) = \frac{1}{\sqrt{n_0}}\sqrt{\frac{\Gamma}{2}\left(\frac{1}{(1+r_{ss}^2)}\right)}$, the equations can be written in a very compact form

$$\frac{d}{dt}\begin{pmatrix}\delta r \\ \delta z\end{pmatrix} = \underbrace{\begin{pmatrix}\tilde{\Gamma}(r_{ss}) & -g \\ g & -\tilde{\Gamma}(z_{ss})\end{pmatrix}}_{A}\begin{pmatrix}\delta r \\ \delta z\end{pmatrix} + \begin{pmatrix}\sqrt{\tilde{D}(r_{ss})}\xi(t) \\ 0\end{pmatrix}. \tag{5.76}$$

The solution of this differential equation is

$$\begin{pmatrix}\delta r \\ \delta z\end{pmatrix}(t) = \int_0^t e^{A(t-t')}\begin{pmatrix}\sqrt{\tilde{D}(r_{ss})}\xi(t') \\ 0\end{pmatrix}dt'. \tag{5.77}$$

The deviation from the classical steady state solution for the second oscillator reads

$$\delta z(t) = \sqrt{\tilde{D}(r_{ss})}\frac{2g}{\omega}\int_0^t \xi(t')e^{\frac{1}{2}(\tilde{\Gamma}(r_{ss})-\tilde{\Gamma}(z_{ss}))(t-t')}\sinh\left(\frac{1}{2}\omega(t-t')\right)dt' \tag{5.78}$$

with $\omega = \sqrt{(\tilde{\Gamma}(r_{ss}) + \tilde{\Gamma}(z_{ss}))^2 - 4g^2}$.

As a next step we calculate the quadratic expectation value

$$\left\langle\delta z^2(t)\right\rangle = D(r_{ss})\frac{4g^2}{\omega^2}\int_0^t\int_0^t dt'dt''\underbrace{\left\langle\xi(t')\xi(t'')\right\rangle}_{\delta(t'-t'')}e^{\frac{1}{2}(\tilde{\Gamma}(r_{ss})-\tilde{\Gamma}(z_{ss}))(t-t')}e^{\frac{1}{2}(\tilde{\Gamma}(r_{ss})-\tilde{\Gamma}(z_{ss}))(t-t'')}$$

$$\times \sinh\left(\frac{1}{2}\omega(t-t')\right)\sinh\left(\frac{1}{2}\omega(t-t'')\right)$$

$$= D(r_{ss})\frac{4g^2}{\omega^2}\int_0^t dt'e^{(\tilde{\Gamma}(r_{ss})-\tilde{\Gamma}(z_{ss}))(t-t')}\sinh^2\left(\frac{1}{2}\omega(t-t')\right)$$

$$= \frac{4g^2}{\omega^2}\frac{e^{-\tilde{\Gamma}(z_{ss})}(2e^{\tilde{\Gamma}(z_{ss})}\omega + 2e^{\tilde{\Gamma}(r_{ss})}(-\omega\cosh(\frac{\omega t}{2}) + 2(\tilde{\Gamma}(r_{ss}) - \tilde{\Gamma}(z_{ss}))\sinh(\frac{\omega t}{2})))}{4(\tilde{\Gamma}(r_{ss}) + \tilde{\Gamma}(z_{ss}))^2 - \omega^2}. \tag{5.79}$$

As we are interested in the steady state, we take the limit $t \to \infty$ and insert the analytical steady state solutions of the symmetry broken regime (Equation 5.61 and Equation 5.62)

$$\lim_{t\to\infty}\left\langle\delta z^2(t)\right\rangle = \frac{g\Gamma^3(\Gamma - 2g - \sqrt{\Gamma^2 - 4\Gamma g})}{4n_0(\Gamma^2 - 4\Gamma g)^{5/2}}. \tag{5.80}$$
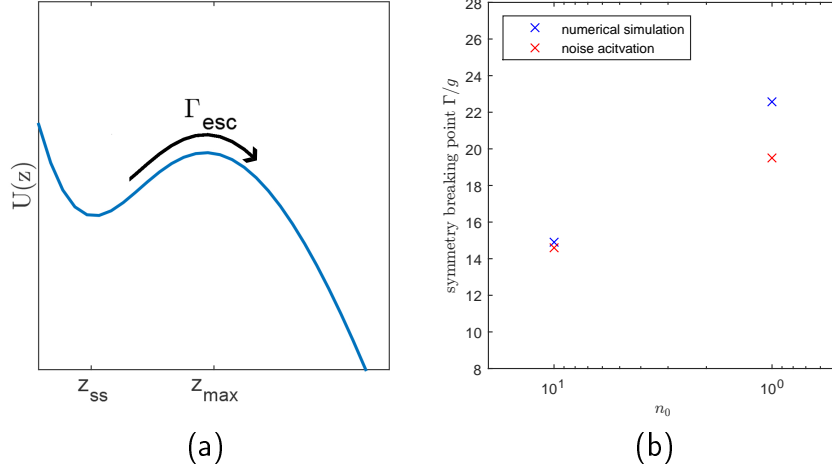
Figure 5.16: (a) Effective potential for the amplitude $z = |\beta|$ of the loss mode for $\Gamma/g = 10$. (b) Dependence of the symmetry breaking point on n_0. The results of the numerical simulations and predictions of our analytical model are compared. For low noise (large n_0 there is very good agreement, while for high noises (i.g. $n_0 = 1$ there are small deviations, due to only considering linear terms in the analytical model.

Although the second oscillator does not directly experience any noise, we can assign an effective noise and moreover an effective temperature through the coupling to the other oscillator

$$N_{eff} = \lim_{t\to\infty} \left\langle \delta z^2(t) \right\rangle. \tag{5.81}$$

We consider the second oscillator (the loss mode) in the the $\mathcal{PT}$-symmetry broken regime and assume that $r = r_{ss}$ and $\phi = \frac{\pi}{2}$ are fixed. Furthermore we neglect the overall loss κ. The remaining equation of motion for the z coordinate reads

$$dz = -\frac{\partial}{\partial z}U_z(z)dt + \sqrt{\Gamma N_{eff}}dW \tag{5.82}$$

where

$$U_z(z) = -\frac{\Gamma}{4(1 + z^2)} - gr_{ss}z \tag{5.83}$$

is the potential of this system (Figure 5.16a). In our parameter regime of interest we find the maximum of the potential at

$$z_{max} \approx 2 - 4gr_{ss}/\Gamma \tag{5.84}$$

while the minimum of the potential equals the classical steady state solutions $z_{min} = z_{ss}$. The potential difference between the minimum and the maximum

of the potential reads

$$\Delta U_z = U_z(z_{max}) - U_z(z_{ss}). \tag{5.85}$$

For a potential like $U_z(z)$ it is possible to escape from the local minimum (steady state solution) over the barrier by thermal activation. From the standard solution for the escape over a single barrier (Kramer's problem) we obtain for the escape rate [17]

$$\Gamma_{esc} \simeq \Gamma_0 e^{-\frac{2\Delta U}{\Gamma N_{eff}}} \tag{5.86}$$

where the prefactor is

$$\Gamma_0 = \sqrt{\frac{-U_z''(z_{ss})U_z''(z_{max})}{4\pi^2}}. \tag{5.87}$$

This rate Γ_{esc} increases as Γ/g is reduced and if the rate exceeds the rate of overall damping κ, the $\mathcal{PT}$-symmetry broken state is not stable and the states can become $\mathcal{PT}$-symmetric. From this we can conclude that the $\mathcal{PT}$-symmetry breaking point is at $\Gamma_{esc} \approx \kappa$. The results are in good agreement with the simulations (Figure 5.16b). For higher noise (small n_0) there are small deviations, which can be attributed to the consideration of only linear terms.

5.3 Comparison of the results obtained by the quantum trajectories method and stochastic differential equations

We now compare the results (see Figure 5.17) for coupled phonon lasers ($\nu = 2$) obtained by solving the master equation using the quantum trajectories method and by making an classical approximation to set up and simulate stochastic differential equations. While for $n_0 = 10$ there is very good agreement of the two methods in the symmetry broken regime where the populations of the systems experience only minor fluctuations, the results differ in the symmetric regime. In the symmetric regime the occupation of the system strongly fluctuates and the classical approximation used holds only true in the low fluctuation limit.

For $n_0 = 1$ different results in the symmetric regime are obtained by the two methods. Even near the breaking point in the broken regime the results differ, nevertheless the two cases approach each other for ever higher Γ/g.

Although there are some differences in the symmetric regime, for both methods the occupations as a function of Γ/g are quite comparable. Moreover, the ratio between the occupation and its variance is similar.

The results obtained by the quantum trajectories method do not show a sharp phase transition as the solutions of the stochastic differential equations and the transition takes place over a wider range of Γ/g. Nevertheless, the $\mathcal{PT}$-symmetry breaking happens at approximately the same Γ/g for both methods.
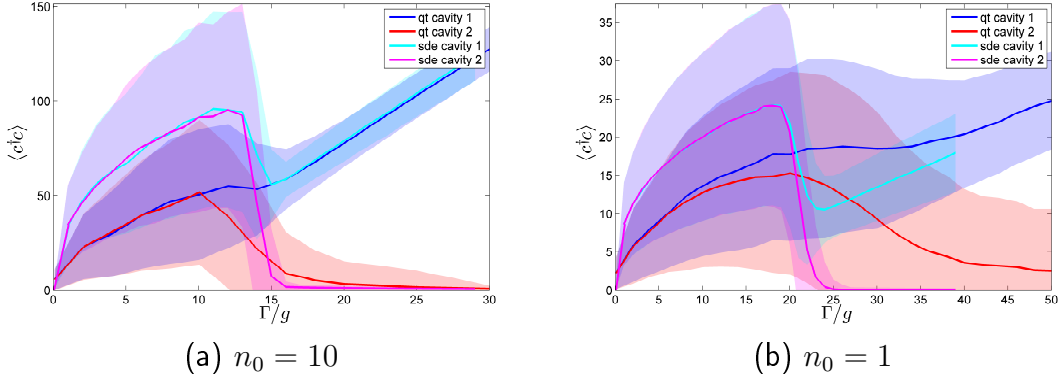
(a) $n_0 = 10$ (b) $n_0 = 1$

Figure 5.17: Comparison of the results for coupled phonon lasers ($\nu = 2$) obtained by solving the master equation by the quantum trajectories method and by making a classical approximation to set up and simulate stochastic differential equations. For $n_0 = 10$ the populations differs for the two methods in the symmetric regime while there is very good agreement in the classical broken regime. For $n_0 = 1$ different results in the symmetric regime are obtained by the two methods. Even near the breaking point in the broken regime the results differ, nevertheless the agreement improves for ever higher Γ/g. The differences result from the use of a classical approximation which is not valid when there is high uncertainty as in the symmetric regime.

5.4 Array of coupled harmonic oscillators

We consider an array of N coupled harmonic oscillators where the first one experiences non-linear gain Γ and the last one the same amount non-linear loss Γ. Moreover, there is an overall linear loss 2κ. The master equation of this $\mathcal{PT}$-symmetric system reads:

$$\dot{\rho} = -\frac{i}{\hbar}[\mathcal{H}, \rho] + \frac{\Gamma}{2}\mathcal{D}[c_g^\dagger]\rho + \frac{\Gamma}{2}\mathcal{D}[c_l]\rho + \kappa \sum_{i=1}^{N} \mathcal{D}[c_i]\rho \tag{5.88}$$

where $c_g^\dagger = c_1^\dagger \frac{1}{\left(1+\frac{c_1^\dagger c_1}{n_0}\right)^{\nu/2}}$ and $c_l = \frac{1}{\left(1+\frac{c_N^\dagger c_N}{n_0}\right)^{\nu/2}} c_N$. The Hamiltonian in rotating frame with respect to ω reads

$$\mathcal{H} = g\left(\sum_{i=1}^{N-1} c_i^\dagger c_{i+1} + c_i c_{i+1}^\dagger\right). \tag{5.89}$$

Solving the master equation Equation 5.88 with quantum trajectories is not reasonable feasible. Nevertheless we can make a classical approximation and derive stochastic differential equations. As we have demonstrated $\mathcal{PT}$-symmetry breaking

for a phonon laser, we focus our analysis on $\nu = 2$. The corresponding Ito equations are

$$d\alpha_1 = -ig\alpha_2 dt + \left(-\kappa + \frac{\frac{\Gamma}{2}}{(1 + \frac{|\alpha_1|^2}{n_0})^\nu}\right)\alpha_1 dt + \frac{\sqrt{\frac{\Gamma}{2}}}{(1 + \frac{|\alpha_1|^2)^{\nu/2}}{n_0})}dW \qquad (5.90)$$

$$d\alpha_i = -ig\alpha_{i-1}dt - ig\alpha_{i+1}dt - \kappa\alpha_i dt \qquad (5.91)$$

$$d\alpha_N = -ig\alpha_{N-1}dt + \left(-\kappa + \frac{\frac{\Gamma}{2}}{(1 + \frac{|\alpha_N|^2}{n_0})^\nu}\right)\alpha_N dt \qquad (5.92)$$

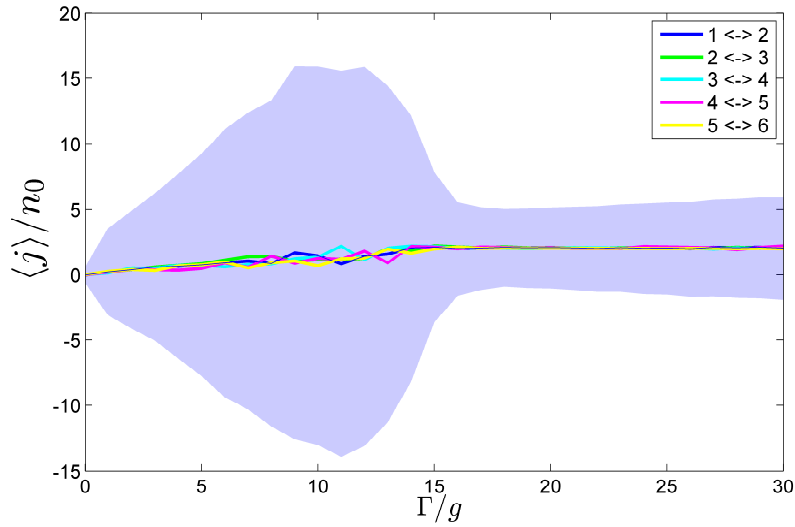with $dW = (dW_1 + idW_2)$ where dW_i are Wiener increments.

Results of numerical simulations of these stochastic differential equations for an array of 6 coupled harmonic oscillators in the classical regime $n_0 = 10$ show that for low Γ/g the system is $\mathcal{PT}$-symmetric (Figure 5.18). The oscillator 1 and 6, 2 and 5, 3 and 4 experience the same population. At $\Gamma/g \approx 14$ this symmetry suddenly changes and the populations of system 1, 3 and 5 agrees with the classical solution of the gain mode and 2, 4 and 6 with the loss mode of the two coupled oscillators (Equation 5.43 and Equation 5.44).

In section 3.4 we figured out that the symmetric regime is governed by the overall loss κ while in the symmetry broken regime the overall loss κ hardly influences the occupation of the system. From Equation 5.91 in steady state and neglecting κ it follows that $\alpha_{i-1} = -\alpha_{i+1}$. Therefore we can conclude that in the symmetry broken regime where κ is negligible, the amplitudes of every second oscillator are equal. This explains why in the symmetry broken region the occupation in the system 1,3 and 5 and 2,4 and 6 are approximately the same.

Moreover there is a significant drop of uncertainty at the breaking point. While there is lots of uncertainty in the symmetric regime, the system can be described as coherent states in the symmetry broken regime. The significant drop of fluctuations is also identified by looking at the current as a function of Γ/g. The mean of the current increases linearly in Γ/g until the breaking point and then remains constant. Moreover the currents between different the oscillators are comparable.
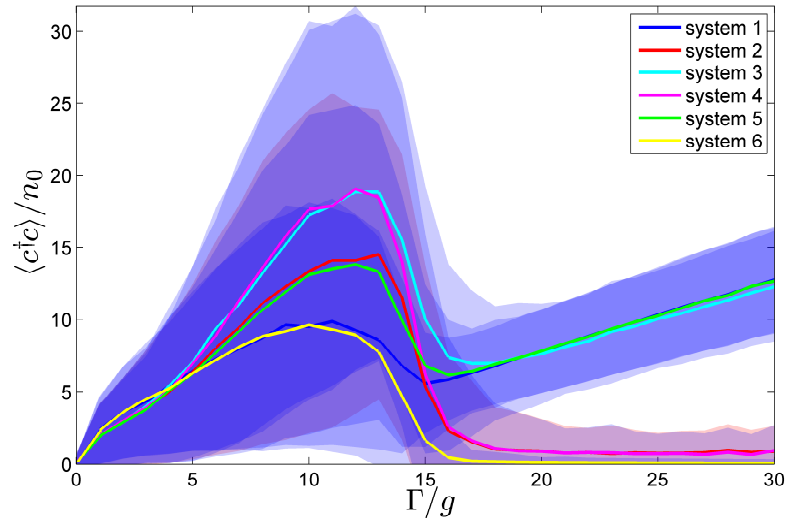
Figure 5.18: Results of numerical simulation of stochastic differential equations for an array of 6 coupled harmonic oscillators, where the first one experience non-linear gain ($\nu = 2$) and the last one experience non-linear loss ($\nu = 2$) both for the classical regime $n_0 = 10$. (a) For low Γ/g the system is $\mathcal{PT}$-symmetric. The oscillator pairs 1 and 6, 2 and 5, 3 and 4 experience the same population. At $\Gamma/g \approx 14$ this symmetry suddenly changes and the populations of system 1, 3, 5 and 2, 4, 6 coincide. Moreover there is a significant drop of uncertainty at the breaking point. The significant drop of fluctuations is also identified by looking at the current as a function of Γ/g (b). The mean of the current increased linearly in Γ/g until the breaking point and then remains constant. Moreover the currents between the oscillators are comparable.

Part II

$\mathcal{PT}$-symmetric spin chains

6 Theoretical Framework

6.1 Matrix Product States

6.1.1 Definition

One of the biggest challenges in quantum many-body physics is the exponential growth of the dimension of the Hilbert space with the number of particles. For N spin 1/2 particles, the dimension of the Hilbert space is 2^N. Storing a 30 spins state in single precision complex numbers would already require 64Gbytes of storage. While storing 30 spins could still be possible on a good computer, storing the full Hilbert space of 300 spins will never be computationally feasible, not even in the future with the best computers as the dimension of the Hilbert space would be $2^{300} \approx 10^{90}$, which is even larger than the number of atoms in the universe. One possibility to circumvent this problem very efficiently in 1D is the use of Matrix Product States (MPS) [21, 22, 23].

Lots of systems in nature are such that the interactions between different particles tend to be local (only nearest neighbor interaction). This locality turns out to the have important consequences. One can show that low-energy eigenstates of gapped Hamiltonians with local interactions obey the so called area-law for the entanglement entropy [24]. The entanglement of a region of space tends to scale as the size of the boundaries of the region and not as the volume. In other words in the case of large 1D systems only a small part of the huge Hilbert space is relevant to describe a quantum state of a local Hamiltonian. Matrix Product States are a method that takes advantage of the area-law such that ground states and time evolution of spin 1/2 chains exceeding 100 spins can be very efficiently and accurately calculated.

A general many-body quantum state may be written as

$$|\Psi\rangle = \sum_{i_1,i_2,..}^{d} \Psi_{i_1,i_2,..}|i_1, i_2, ..\rangle \tag{6.1}$$

and has the Hilbert space dimension of d^N where d is the dimension of the one particle Hilbert space ($d = 2$ for a spin 1/2 system) and N the number of particles. This state can be rewritten as a Matrix Product State

$$|\Psi\rangle = \sum A_i^{1,\alpha} A_j^{\alpha,\beta} A_k^{\beta,\gamma}....|i, j, k, ...\rangle \tag{6.2}$$

where $A_j^{\alpha,\beta}$ is rank 3 tensor, where the latin letter is the physical index referring to the single particle state ($j = 1, .., d$), while the greek letters are the virtual indices with the so called bond dimension D. The bond dimension can be interpreted as a measure of entanglement (details can be found in the examples). In the following, we use a short hand notation

$$|\Psi\rangle = \sum A_i^1 A_j^2 A_k^3 ..... |i, j, k, ...\rangle \quad (6.3)$$

where A_i is a $D \times D$ matrix.

For better understanding, we introduce a graphical notation (see Figure 6.1). A box represents a tensor, the number of lines in contact with the box define the rank of the tensor. Again, latin letters define physical indices, while the greek letters define virtual indices. The number of open lines denotes the number of free indices of the tensor. If there are no open lines, the boxes describe a scalar.

Examples

Further insight into the meaning of the bond dimension can be gained by looking at some examples of MPS: First of all, we consider a simple product state $|010\rangle$ with the corresponding MPS

$$\begin{aligned} A_0^1 = 1, A_0^2 = 0, A_0^3 = 1 \\ A_1^1 = 0, A_1^2 = 1, A_1^3 = 0. \end{aligned} \quad (6.4)$$

In this example the bond dimension $D = 1$.

As a next step we focus on entangled states represented as Matrix Product States. The MPS state of the GHZ-state $|000\rangle + |111\rangle$ (unnormalized for simplicity) is

$$\begin{aligned} A_0^1 = \begin{pmatrix} 1 & 0 \end{pmatrix}, A_0^2 = \begin{pmatrix} 1 & 0 \\ 0 & 0 \end{pmatrix}, A_0^3 = \begin{pmatrix} 1 \\ 0 \end{pmatrix} \\ A_1^1 = \begin{pmatrix} 0 & 1 \end{pmatrix}, A_1^2 = \begin{pmatrix} 0 & 0 \\ 0 & 1 \end{pmatrix}, A_1^3 = \begin{pmatrix} 0 \\ 1 \end{pmatrix}. \end{aligned} \quad (6.5)$$

Here in the case of an entangled state the bond dimension equals $D = 2$. For the W-state $|100\rangle + |010\rangle + |001\rangle$ (unnormalized for simplicity), we also get a bond dimension of $D = 2$.

$$\begin{aligned} A_0^1 = \begin{pmatrix} 1 & 0 \end{pmatrix}, A_0^2 = \begin{pmatrix} 1 & 0 \\ 0 & 1 \end{pmatrix}, A_0^3 = \begin{pmatrix} 0 \\ 1 \end{pmatrix} \\ A_1^1 = \begin{pmatrix} 0 & 1 \end{pmatrix}, A_1^2 = \begin{pmatrix} 0 & 1 \\ 0 & 0 \end{pmatrix}, A_1^3 = \begin{pmatrix} 1 \\ 0 \end{pmatrix}. \end{aligned} \quad (6.6)$$
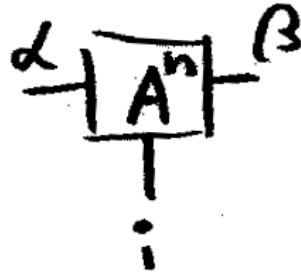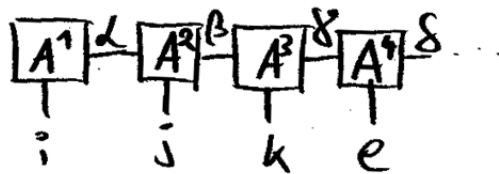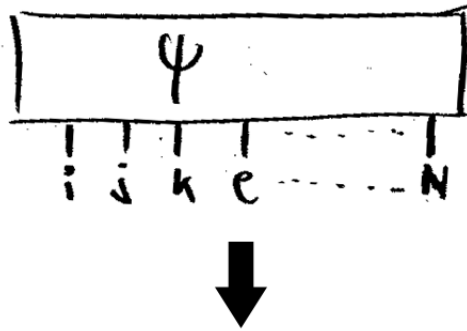
(a) A^n in graphical notation

(b) $|\psi\rangle$ in full Hilbert space and as MPS

Figure 6.1: a) Graphical notation of a tensor: A box represents a tensor, the number of lines in contact with the box define the rank of the tensor. Latin letters are always used for the physical index, while the greek letters represent virtual indices. b) Graphical notation of the state $|\Psi\rangle$ in the full Hilbert space and as a Matrix Product State.
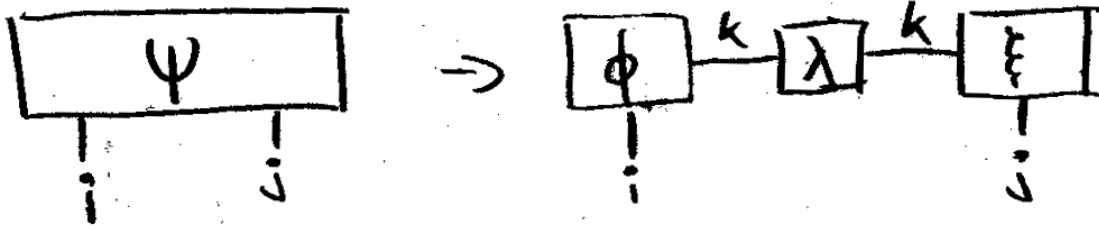
Figure 6.2: The Schmidt decomposition is a way of expressing a state $|\psi\rangle$ as a tensor product of the two inner product spaces $|\phi\rangle$ and $|\xi\rangle$ where λ are the weighting factors.

6.1.2 Schmidt decomposition

The Schmidt decomposition is a way of expressing a state $|\psi\rangle$ as a tensor product of the two inner product spaces $|\phi_k\rangle$ and $|\xi_k\rangle$ where λ_k are the weighting factors and m is the Schmidt number:

$$|\Psi\rangle = \sum_{i,j}^{d} \Psi_{i,j}|i,j\rangle = \sum_{k=1}^{m} \lambda_k|\phi_k\rangle|\xi_k\rangle \qquad (6.7)$$

If an entangled state can be decomposed as a sum of product states, the Schmidt number is greater than one. The dimension of the state $|\Psi\rangle$ is d^2 while the dimension of the decomposed state is $2md$. For small Schmidt numbers (low entanglement) this representation needs less numbers to store. The Schmidt decomposition can be implemented on a computer very efficiently via a QR-algorithm [25]. Furthermore, the Schmidt decomposition can be easily expressed in the graphical notation (see Figure 6.2). The Schmidt decomposition has the following properties:
Each product space forms an orthogonal basis

$$\langle\phi_i|\phi_j\rangle = \delta_{ij} \qquad (6.8)$$

$$\langle\xi_i|\xi_j\rangle = \delta_{ij}. \qquad (6.9)$$

In general, the two subspaces need not to be similar

$$\dim(\phi) \neq \dim(\xi). \qquad (6.10)$$

In the case of normalized quantum states we can derive another property:

$$\rho^1 = \text{Tr}_2(|\Psi\rangle\langle\Psi|) = \sum_{k}^{m} \lambda_k^2|\phi_k\rangle\langle\phi_k|, \qquad (6.11)$$

$$\text{Tr}(\rho) = 1 \Rightarrow \sum_{k=1}^{m} \lambda_k^2 = 1. \qquad (6.12)$$

The Schmidt decomposition is equivalent to the singular value decomposition (SVD) where an $n \times n$ matrix M is decomposed into an $n \times n$ unitary matrix U, an $n \times m$ diagonal matrix Σ and an $m \times m$ unitary matrix V.

$$M = U\Sigma V^*. \tag{6.13}$$

6.1.3 Truncation

In order to keep the amount of data that has to be stored as little as possible and still obtain accurate results, one may only keep the n largest Schmidt weights that fulfill

$$\sum_{k=1}^{n} \lambda_k^2 < (1 - \epsilon) \sum_{k=1}^{m} \lambda_k^2 \text{ and } n < D_{max} \tag{6.14}$$

where ϵ is the truncation error and D_{max} the maximum bond dimension. One usually chooses a truncation error of 10^{-6}. The maximum bond dimension D_{max} has a polynomial dependence on the number of particles N. For pure states of spin 1/2, D_{max} can be estimated simply as N.

6.1.4 Vector $\leftrightarrow$ MPS

In Figure 6.3 we see how an arbitrary state can be transformed to a Matrix Product State. We start with the arbitrary state $|\Psi\rangle$ which is d^N-dimensional. First of all, we reshape the state to a $d \times d^{N-1}$ matrix. Secondly, we perform a Schmidt decomposition and get A^1 and contract the Schmidt weights λ with B to get the new tensor $\tilde{B}$. The dimension between A^1 and $\tilde{B}$ is D. As a next step, the tensor $\tilde{B}$ is reshaped to a $Dd \times d^{N-2}$ matrix and a Schmidt decomposition is performed. This goes on until we end up with a scalar in the Schmidt decomposition, or equivalently have A^i for $i = 1$ to N.

The transformation of a Matrix Product State into an N dimensional tensor can be done by contracting the MPS over all virtual indices

$$\sum_{\alpha,\beta,\gamma,\dots} A_{1,\alpha}^i A_{\alpha,\beta}^j A_{\beta,\gamma}^k \dots = \Psi_{i,j,k,\dots}. \tag{6.15}$$

6.1.5 Scalar products and expectation values

In Figure 6.4 we see what scalar products and expectation values in the graphical notation look like. The bar over A in the bra vectors denotes the complex conjugate of A. As mentioned before, there are no open lines in scalar products and expectation values and the output in both cases is just a complex number.

(a) $|\Psi\rangle$

(b) reshape Ψ

(c) perform Schmidt decomposition

(d) contract λ^1 and B to $\tilde{B}$

(e) reshape $\tilde{B}$

(f) perform Schmidt decomposition

(g) contract λ^2 and C to $\tilde{C}$
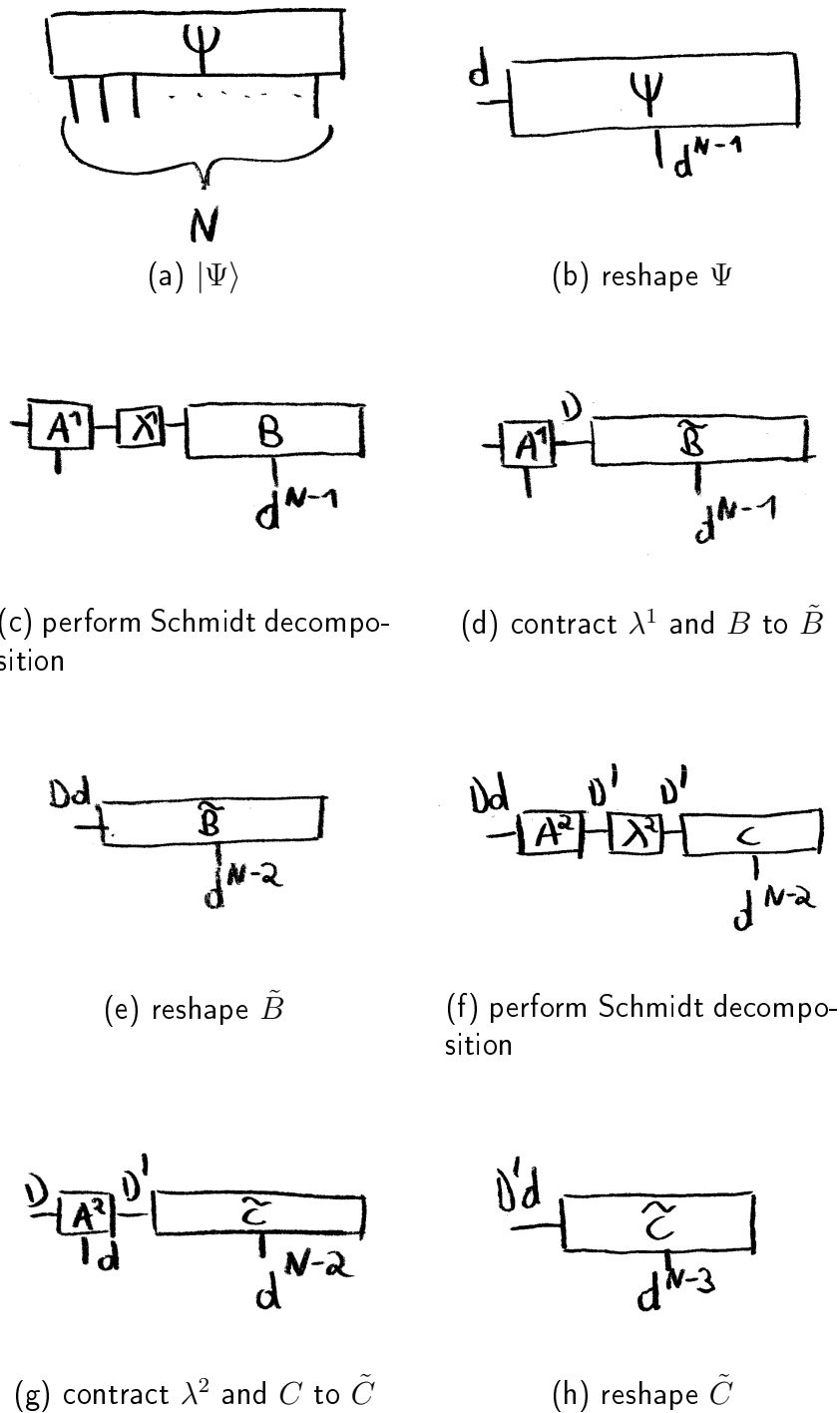
(h) reshape $\tilde{C}$

Figure 6.3: a) We start with the arbitrary state $|\Psi\rangle$ which is d^N dimensional. b) We reshape the state to a $d \times d^{N-1}$ matrix. c) We perform a Schmidt decomposition and get A^1 and then d) contract the Schmidt weights λ with B to get the new tensor $\tilde{B}$. The dimension between A^1 and $\tilde{B}$ is D. e) As a next step the tensor $\tilde{B}$ is reshaped to a $Dd \times d^{N-1}$ matrix. f) a Schmidt decomposition is performed. This goes on until we end up with a scalar in the Schmidt decomposition or, equivalently, if we have A^i for $i = 1$ to N.

(a) $|\theta\rangle$ (b) $\langle\Psi|$

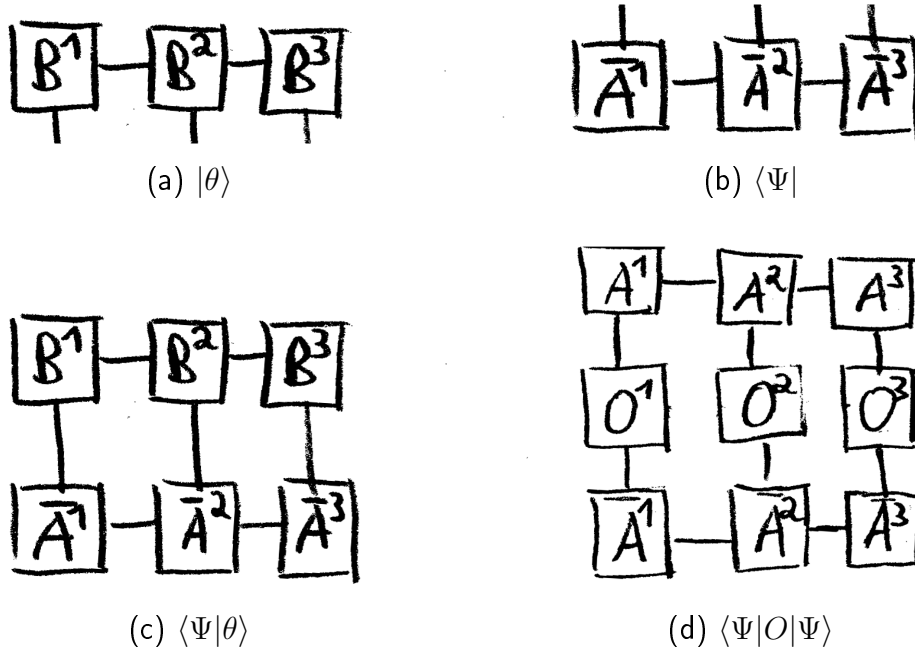(c) $\langle\Psi|\theta\rangle$ (d) $\langle\Psi|O|\Psi\rangle$

Figure 6.4: Matrix product state representation of a) ket state $|\theta\rangle$ and b) bra state $\langle\Psi|$. c) Scalar product $\langle\theta|\Psi\rangle$ and d) expectation value of an Operator O $\langle\Psi|O|\Psi\rangle$.
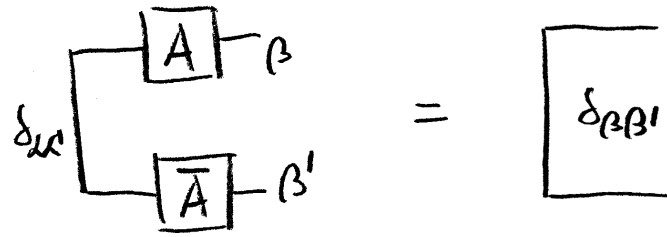
6.1.6 Canonical form

The Matrix Product State representation is not unique. One can easily show that by inserting the unity $\mathbb{1} = XX^{-1}$

$$|\Psi\rangle = \sum A_i^1 A_j^2 A_k^3 .....|i, j, k, ...\rangle =$$
$$\sum A_i^1 X_1 X_1^{-1} A_j^2 X_2 X_2^{-1} A_k^3 X_1 X_1^{-1} .....|i, j, k, ...\rangle = \qquad (6.16)$$
$$\sum \tilde{A}_i^1 \tilde{A}_j^2 \tilde{A}_k^3 .....|i, j, k, ...\rangle.$$

We can always perform such a transformation that makes all elements unity on the left/right side of a tensor when calculating a scalar product or expectation value [26]. We say it is left/right canonical (see Figure 6.5). This is very often called the normal form. If an MPS is left canonical with respect to site N, one can simply calculate the norm by contracting the tensor A_N with its complex conjugate. It is also possible to make an MPS left and right canonical with respect to a certain site. If one wants to calculate a local expectation value of this specific site i, the tensor of that site A_i, the operator O and the $\bar{A}_i$ have to be contracted (see Figure 6.6).

Transforming an MPS into the canonical form can be done by a singular value decomposition (subsection 6.1.2). If we want to have a left canonical MPS, we perform a singular value decomposition on the first tensor A^1 and get a unitary

(a) left canonical
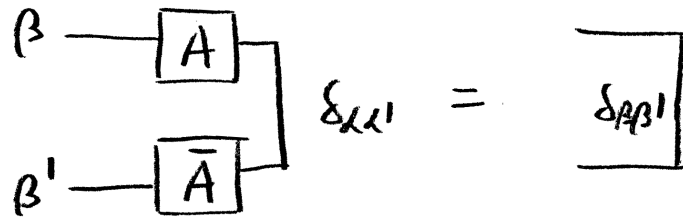
(b) right canonical

Figure 6.5: Canoncial/Normal form.

matrix (see Equation 6.8) and then contract the diagonal matrix with the Schmidt weights and the other unitary matrix with the next tensor. Then we perform a singular value decomposition on the next tensor and so on. This way, all tensors except the last one are equal to unity. One can do the same procedure starting at the Nth tensor and moving to the left in order to make a state right canonical.

6.1.7 Minimization

As explained at the beginning of the MPS chapter, MPS only uses a part of the full Hilbert space. After performing several time evolution steps, the bond dimension will usually exceed the maximum bond dimension. Instead of just throwing away all information exceeding the maximum bond dimension, we want to find the best approximation within our part of the Hilbert space.
Therefore, we solve a minimization problem:

$$min \left\| \Psi_{D_{max}} - \theta_D \right\|^2 \tag{6.17}$$

where D is the bond dimension of the state $|\theta\rangle$ of which we want to find the best approximation Ψ with the bond dimension D_{max}. This can be achieved by using the variational principle. Therefore, the problem that should be minimized is varied with respect to Ψ^* and set to zero.

$$\frac{\partial}{\Psi^*}(\langle\Psi|\Psi\rangle - \langle\Psi|\theta\rangle) = 0 \tag{6.18}$$

(a) local expectation value on site 2
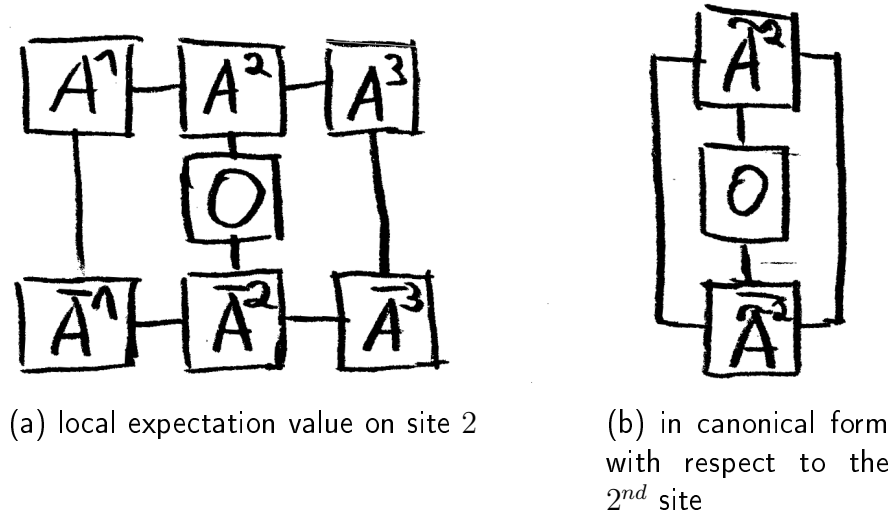
(b) in canonical form with respect to the 2nd site

Figure 6.6: Expectation value of an operator acting on site 2 a) in an abitrary form and b) in canonical form.

In the case of Matrix Product States we get a set of equations

$$\frac{\partial}{\partial \bar{A}^n}(\langle \Psi | \Psi \rangle - \langle \Psi | \theta \rangle) = 0 \text{ or equivalently } \frac{\partial}{\partial \bar{A}^n}\langle \Psi | \Psi \rangle = \frac{\partial}{\partial \bar{A}^n}\langle \Psi | \theta \rangle. \qquad (6.19)$$

This differentiation is equivalent to calculating the scalar product without the tensor that is differentiated (graphical notation Figure 6.7). Furthermore, we look at the graphical notation of the minimization problem (Equation 6.19) in canonical form (Figure 6.8). The tensors R and L denote the contraction of all tensors to the right and left of the scalar product. By differentiating and setting it to zero it follows that the contraction of L_i, B^i and R_i equals the tensor A^i. We therefore replace the old A^i tensor of the MPS with the contraction of L_i, B^i and R_i. A good approximation can be achieved by sweeping from $i = 1$ to N and back and calculating all A^i until $\langle \Psi | \Psi \rangle - \langle \Psi | \theta \rangle <$ error tolerance. The error tolerance is usually in the order of 10^{-8}, pointing out how efficient this method is.

This is a one-site algorithm, where only one site is updated each time. If the first approximation $|\Psi\rangle$ before the optimization is a product state with a bond dimension of 1, the bond dimension will always stay one. One way to overcome this problem is to start with a random state with maximum bond dimension. Even then during the calculation the bond dimension between two sites can get less but can never grow. As a result the calculation can get stuck in local minima. To overcome this problem, we can perform a two-sites algorithm where two sites are updated at each time (see Figure 6.8). The new tensor consisting two sites is then Schmidt decomposed and replaces the old tensor. This method is very efficient,
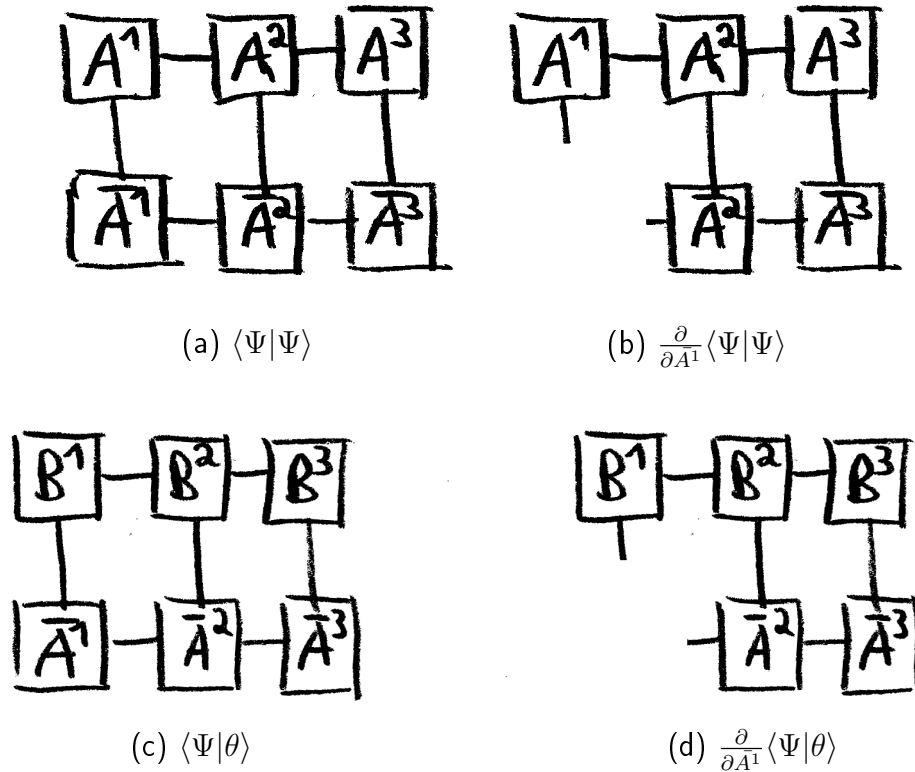
(a) $\langle \Psi | \Psi \rangle$ (b) $\frac{\partial}{\partial \bar{A}^1} \langle \Psi | \Psi \rangle$

(c) $\langle \Psi | \theta \rangle$ (d) $\frac{\partial}{\partial \bar{A}^1} \langle \Psi | \theta \rangle$

Figure 6.7: a) The norm $\langle \Psi | \Psi \rangle$ written as MPS. b) $\frac{\partial}{\partial \bar{A}^1} \langle \Psi | \Psi \rangle$. The differentiation can be done by calculating the scalar product without this tensor that is differentiated. c) The scalar product $\langle \Psi | \theta \rangle$. d) The deriviation of a scalar product $\frac{\partial}{\partial \bar{A}^1} \langle \Psi | \theta \rangle$.

after a few times of sweeping back and forth the minimization converges, and a global minimum can be found. Further iteration does only weakly effect the error of this method.

6.1.8 Time evolution

The fastest and also the easiest way to do the time evolution of a MPS is by the Suzuki-Trotter expansion. Therefore we split the Hamiltonian in even and odd terms

$$H = H_e + H_o = \sum_i^{\frac{N}{2}} h_{2i} + \sum_i^{\frac{N}{2}} h_{2i-1}. \tag{6.20}$$

We perform the time evolution by applying the time evolution operator only to two sites at each time. For this, we use one of the following Trotter expansions:
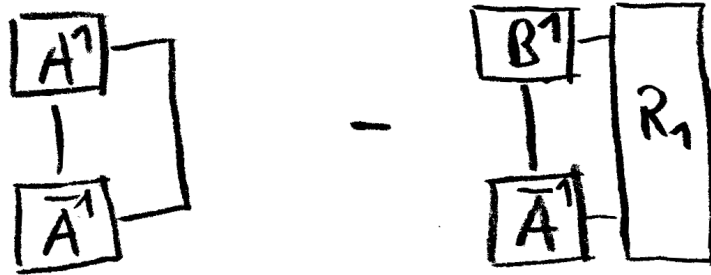
(a) Graphical notation of the minimization problem (Equation 6.19) in canonical form. The tensors R and L denote the contraction of all tensors to the right and left of the scalar product.
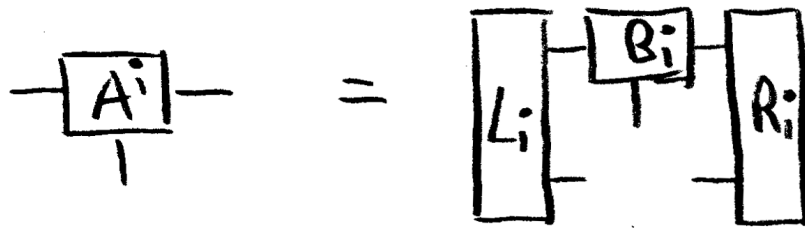
(b) From differentiation of the minimization problem as in (a) and setting it to zero it follows that the new tensor A^i equals the contraction of L_i, B^i and R_i.
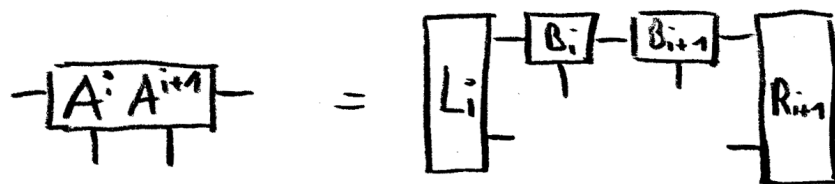
(c) The same algorithm as in (b) but for two-sites. This has the advantage that the bond dimension between the sites can grow during the calculation.

Figure 6.8

1st order Trotter expansion

$$e^{-iH\Delta t} = e^{-iH_e\Delta t}e^{-iH_o\Delta t} + \mathcal{O}(\Delta t). \tag{6.21}$$

2nd order Trotter expansion

$$e^{-iH\Delta t} = e^{-i\frac{1}{2}H_e\Delta t}e^{-iH_o\Delta t}e^{-i\frac{1}{2}H_e\Delta t} + \mathcal{O}(\Delta t^2). \tag{6.22}$$

Forest-Ruth formula

$$e^{-iH\Delta t} = e^{-i\frac{1}{2}\theta H_e\Delta t}e^{-i\theta H_o\Delta t}e^{-i\frac{1}{2}(1-\theta)H_e\Delta t}e^{-i(1-2\theta)H_o\Delta t}$$
$$\times e^{-i\frac{1}{2}(1-\theta)H_e\Delta t}e^{-i\theta H_o\Delta t}e^{-i\frac{1}{2}\theta H_e\Delta t} + \mathcal{O}(\Delta t^5) \tag{6.23}$$

with $\theta = \frac{1}{2-2^{1/3}}$.

Besides Trotter expansions there are several other methods to do time evolution of an MPS:

- Runge-Kutta:
  less accurate than Forest-Ruth formula and slower

- Lanczos/Arnoldi:
  slower, but for big time-steps the only algorithm with reasonable accuracy

- Pade-Approximation:
  the slowest of the algorithms

For a detailed review see [27].

In Figure 6.9 we can see one 1st order Trotter step applied to a Matrix Product State. In Figure 6.10 it is illustrated that the bond dimension after every Trotter step can grow up to a factor of d. By just applying consecutive Trotter steps, very soon the limits of the bond dimension are reached and information will be discarded. To overcome this problem, we approximate the MPS after every time step with the best solution within our maximum bond dimension (see subsection 6.1.7). In other words, after every Trotter time step the state is outside of our Hilbert space and is projected back with nearly the same state inside the MPS Hilbert space. As the tolerance limit of our minimization procedure is low (10^{-8}), the error is negligible but the benefit is huge as time evolution can be done with a lower maximum bond dimension. A higher maximum bond dimension would lead to much longer computation times and storage of large amounts of data.

Time evolution can also be used for ground state search. Therefore we have to replace the time with its negative imaginary time $t \to -it$. This can be clarified by expanding an arbitrary state $|\Psi\rangle$ in the eigenbasis of the Hamiltonian and applying the time evolution operator. All excited states will be more strongly suppressed than the ground state and as a result, only the ground state E_0 will survive,

$$U|\Psi\rangle = e^{-Ht}|\Psi\rangle = e^{-Ht}\sum_n a_n|\phi_n\rangle = \sum_n a_n e^{-E_n t}|\phi_n\rangle. \tag{6.24}$$
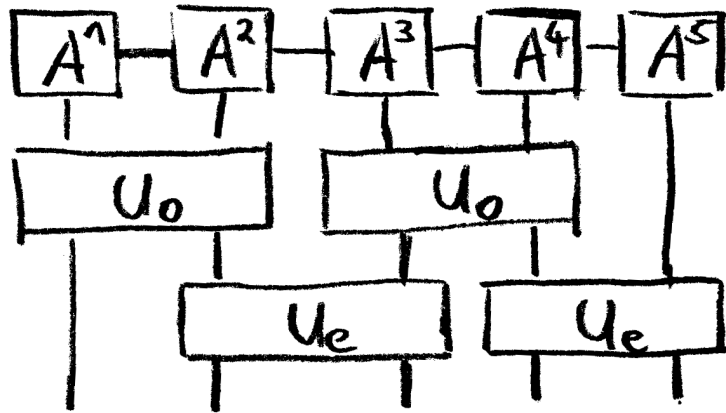
(a) 1st order Trotter
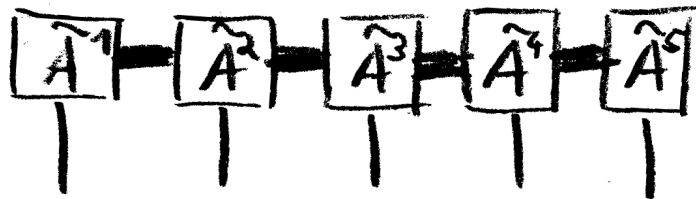
(b) MPS after Trotter step

Figure 6.9: 1st order Trotter algorithm applied on an MPS. After a time step, the bond dimension between the tensors of the MPS has grown. This is indicated by the thicker line between the tensors. For detailed explanation why the bond dimension grows see Figure 6.10.

6.1.9 Matrix Product Operator (MPO)

Not only quantum states can be transferred to a matrix representation, this concept also works for operators. But unlike states, operators have an additional physical index. This can be visualized in the graphical notation (see Figure 6.11). Most of the time we are dealing with local, neighbor or next neighbor interaction and for this class of systems there exists a more or less standard procedure of rewritting a Hamiltonian to a Matrix Product Operator. Therefore we look at some simple examples.

(a) time evolution is applied

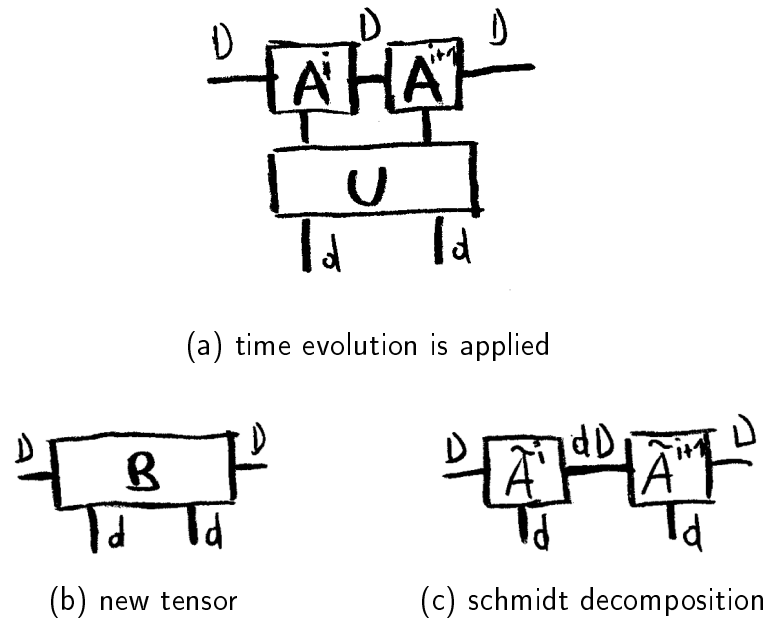(b) new tensor   (c) schmidt decomposition

Figure 6.10: These graphs illustrate that the bond dimension grows after applying a two-site time evolution operator. First, all tensors are contracted. Secondly, the obtained tensor is split into two via Schmidt decomposition. The most a bond dimension can grow in the case of a two-site time evolution operator is the factor d (physical dimension).
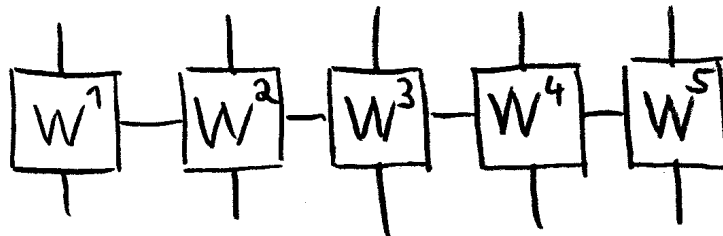
Figure 6.11: Graphical notation of a Matrix Product Operator (MPO).

Examples:

The Ising Hamiltonian

$$H = J \sum_{i=1}^{(N-1)} \sigma_z^i \sigma_z^{i+1} \tag{6.25}$$

can be rewritten as an MPO as

$$W^1 = \begin{pmatrix} 0 & J\sigma_z & \mathbb{1}_2 \end{pmatrix}, W^i = \begin{pmatrix} \mathbb{1}_2 & 0 & 0 \\ \sigma_z & 0 & 0 \\ 0 & J\sigma_z & \mathbb{1}_2 \end{pmatrix}, W^N = \begin{pmatrix} \mathbb{1}_2 \\ \sigma_z \\ 0 \end{pmatrix}. \tag{6.26}$$

As a next step we look at a more complex Hamiltonian:
The XYZ chain Hamiltonian reads

$$H = J \sum_{i=1}^{(N-1)} \sigma_x^i \sigma_x^{i+1} + \sigma_y^i \sigma_y^{i+1} + \sigma_z^i \sigma_z^{i+1} + h \sum_{i=1}^{N} \sigma_z^i \tag{6.27}$$

which can be rewritten as an MPO:

$$W^1 = \begin{pmatrix} h\sigma_z & J\sigma_x & J\sigma_y & J\sigma_z & \mathbb{1}_2 \end{pmatrix}, W^i = \begin{pmatrix} \mathbb{1}_2 & 0 & 0 & 0 & 0 \\ \sigma_x & 0 & 0 & 0 & 0 \\ \sigma_y & 0 & 0 & 0 & 0 \\ \sigma_z & 0 & 0 & 0 & 0 \\ h\sigma_z & J\sigma_x & J\sigma_y & J\sigma_z & \mathbb{1}_2 \end{pmatrix},$$

$$W^N = \begin{pmatrix} \mathbb{1}_2 \\ \sigma_x \\ \sigma_y \\ \sigma_z \\ h\sigma_z \end{pmatrix}. \tag{6.28}$$

6.1.10 Density Matrix Renormalization Group (DMRG)

Very often, we are interested in finding the ground state of a given system. We can do this by using the variational principle. Therefore we define the energy functional $E[\Psi]$ we want to minimize

$$E[\Psi] = \frac{\langle \Psi | H | \Psi \rangle}{\langle \Psi | \Psi \rangle}. \tag{6.29}$$

Equivalent to the minimization of the distance between states, we differentiate the functional and set it to zero.

$$\frac{\partial E[\Psi]}{\partial \Psi^*} = 0, \Rightarrow H|\Psi\rangle = E|\Psi\rangle, \tag{6.30}$$

where $|\Psi\rangle$ is the normalized state. As a result we get the Schroedinger equation. In the case of MPS, we do not variate the whole wave function, instead we vary with respect to the tensor A_n of the MPS. Thus,

$$E[A_n] = \frac{A_n^\dagger H_{eff} \vec{A}_n}{\vec{A}_n^\dagger \vec{A}_n}. \tag{6.31}$$

Therefore, we differentiate the function with respect to the tensor A_n and set it to zero:

$$\frac{\partial E[A_n]}{\partial \vec{A}_n^\dagger} = 0, \Rightarrow H_{eff} \vec{A}_n = E_{min} \vec{A}_n \tag{6.32}$$

(a) $\langle\Psi|H|\Psi\rangle$ (b) H_{eff}
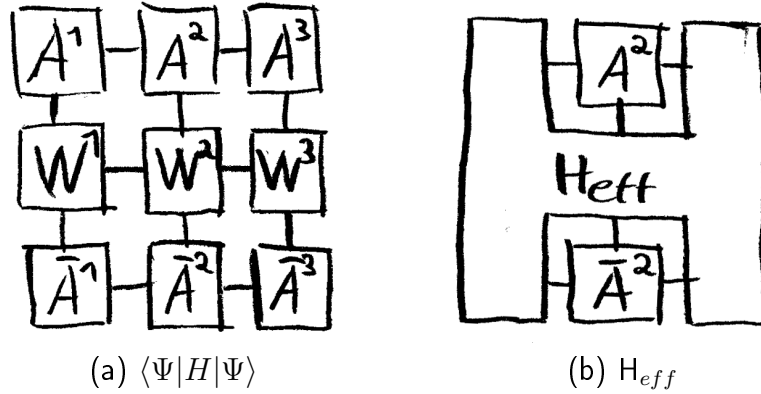
Figure 6.12: a) Expectation value of H b) H_{eff} with respect to site 2. H_{eff} is calculated by contracting all tensors of a) except the tensors A^2 and $\bar{A}^2$.

The minimum of the energy functional can be found by finding the lowest eigenstate of H_{eff} for every site. H_{eff} with respect to site i can be calculated by contracting all tensors of the energy functional except the tensors A^i and $\bar{A}^i$. In Figure 6.12 we see the energy functional and H_{eff} with respect to the 2nd site. The ground state of a Hamiltonian can be calculated by finding the lowest eigenstate of H_{eff} with respect to site i and replace the A^i with it for every site. This needs to be done back and forth until the expectation value of $\langle E\rangle$ converges. The lowest eigenstate of H_{eff} can be efficiently calculated with the Arnoldi algorithm, which is similar to the Lanczos algorithm but can be used for non-Hermitian matrices.

Again, this procedure can be improved by doing a two-site algorithm in order to allow the bond dimension to grow between different sweeps. This can done equivalently to subsection 6.1.7.

6.1.11 Open quantum systems

A system can never be completely screened from its environment and as a result there are only open quantum systems in nature. A way to introduce this coupling to the environment is the master equation (see section 3.1). In order to simulate open quantum systems with MPS we 'vectorize' the density matrix. This can be done by reshaping the matrix into a vector. As a consequence, we also have to transform the master equation. We use the following transformation rules for an arbitrary operator A:

$$A\rho \rightarrow (A \otimes 1)|\rho\rangle \tag{6.33}$$

and

$$\rho A \rightarrow (1 \otimes A^T)|\rho\rangle \tag{6.34}$$

Example

A master equation for a simple dissipative system with the loss rate Γ reads

$$\dot{\rho} = \frac{\Gamma}{2}(2a\rho a^\dagger - a^\dagger a\rho - \rho a^\dagger a) \tag{6.35}$$

and can be rewritten into the following 'vectorized' form

$$\frac{d}{dt}|\rho\rangle = \frac{\Gamma}{2}(2a \otimes (a^\dagger)^T - a^\dagger a \otimes 1 - 1 \otimes (a^\dagger a)^T)|\rho\rangle. \tag{6.36}$$

This equation can be written in short as $\frac{d}{dt}|\rho\rangle = L|\rho\rangle$, where L is the Liouvillian operator.

By vectorizing the density matrix and transforming the master equation, we can simulate open quantum systems the same way as in the non-dissipative case but the physical index changes $d \to d^2$. In addition, expectation values can not be calculated by $\langle\Psi|O|\Psi\rangle$ as the state has not to be pure any more. Expectation values are calculated by $\mathrm{Tr}\,(\rho O)$. This can be achieved by calculating the scalar product between the density ρ and the operator O. In Figure 6.13 the expectation value of an operator O acting on site two is sketched in graphical notation.

Often people are only interested in the steady state behavior of an open quantum system. Instead of doing the time evolution a very long time, we can directly calculate the steady state by finding the state to the zero eigenvalue of the Liouvillian operator L.

There basically exist two methods [28, 29]. The first one is to find the ground state of $L^\dagger L$ using the same method as explained in subsection 6.1.10. This is in general more stable. The other possibility is to use the same algorithm as for ground state search on L but always look for the eigenstate closest to zero instead of the lowest on every site. In certain cases this can converge faster, but it is very often numerical unstable.

Moreover it should be noted that the MPS concept can be extend to infinite 1D spin chain [30] or to two dimensions [31].
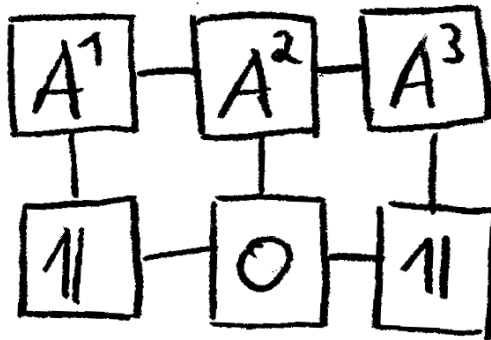
Figure 6.13: Expectation value of an operator O acting on site 2. In open quantum system states are in general not pure and to get the expectation value the scalar product between the density ρ and the operator O has to be calculated.

7 Numerical implementation

7.1 Numerical implementation of MPS

In the following, the subscript of an MPS tensors tensor denotes the site while in the superscript there are the physical as well as the virtual indices of the tensor. Moreover the Einstein summation convention is used.

7.1.1 Minimization Algorithm (two site algorithm)

We want to solve the minimization problem

$$min \, \|\Psi - \theta\|^2 \tag{7.1}$$

where we want to approximate the MPS θ with the state Ψ which usually has a lower bond dimension as explained in subsection 6.1.7. This can be efficiently implemented by this algorithm:

1. Prepare $|\Psi\rangle$ in the right cannonical form with respect to the first site

2. Prepare $|\Theta\rangle$ in the cannonical form (just for numerical stability)

3. Calculate all transfer matrices $R_{[i]}$ from $i = N$ to 1 and $L_{[1]}$. The transfer matrix $R_{[i]}$ is the contraction of all sites on the right of site i of the scalar product.

4. For $k = 1 : (N-1)$

   a) Calculate the new tensor (see Figure 6.8)
   $$\tilde{A}^{\alpha ij\epsilon}_{[k,k+1]} = L^{\alpha\beta}_{[k]} B^{\beta i\gamma}_{[k]} B^{\gamma j\delta}_{[k+1]} R^{\delta\epsilon}_{[k+1]} \tag{7.2}$$

   b) Singular value decomposition with truncation to the maximum bond dimension D_{max}
   $$\tilde{A}^{\alpha ij\delta}_{[k,k+1]} \to \tilde{A}^{\alpha i\beta}_{[k]} \tilde{A}^{\beta j\delta}_{[k+1]} \tag{7.3}$$
   where we choose $\tilde{A}^{\alpha i\beta}_{[k]}$ to be unitary, and replace $A^{\alpha i\beta}_{[k]}$ with $\tilde{A}^{\alpha i\beta}_{[k]}$. In addition, we insert left canonical $\tilde{A}^{\alpha j\beta}_{[k+1]}$ at site $k+1$. As a result, the MPS is in left and right canonical form with respect to the sites $k+1$ and $k+2$.

c) As a next step we update the transfer matrices

$$L_{[k+1]}^{\gamma\delta} = L_{[k]}^{\alpha\beta} A_{[k]}^{\alpha i \gamma} \bar{A}_{[k]}^{\beta i \delta} \tag{7.4}$$

end

5. The same algorithm as in point 4 but adapted to the opposite direction for $k = N$ to 2

6. If the distance $\langle \Psi | \Psi \rangle - \langle \Psi | \theta \rangle >$ tolerance, go to point 4. Else finished

7.1.2 Algorithm for time evolution (2nd order Trotter)

For most problems it is sufficient to use the Suzuki-Trotter expansion up the 2nd order (subsection 6.1.8). In general it is always recommended to use the 2nd order instead of the 1st order method, because the computational costs are nearly the same. The only difference is that at the beginning and the end of the time evolution there is a half time step, as in the second order case all other half time steps add to a full one. After every time step we look for the best approximation with a bond dimension smaller equals D_{max}. Here is an example for a time evolution algorithm of the Hamiltonian H for a state $|\Psi_0\rangle$:

1. Split the Hamiltonian H in even H_e and odd sites H_o

2. Calculate the even site time evolution operator for a full $U_o = e^{-iH_o\Delta t}$ and a half time step $U_{ho} = e^{-i\frac{1}{2}H_o\Delta t}$

3. Calculate the odd site time evolution operator for a full $U_e = e^{-iH_e\Delta t}$ and a half time step $U_{he} = e^{-i\frac{1}{2}H_e\Delta t}$

4. Apply half a time step to the even sites $|\Psi\rangle = U_{he}|\psi_0\rangle$

5. $For l = 1$ to $(N-1)$

   - Apply one time step to the odd sites $|\Psi\rangle = U_o|\Psi\rangle$
   - Apply one time step to the even sites $|\Psi\rangle = U_e|\Psi\rangle$
   - Approximate the state with a state of lower bond dimension than D_{max} by using the algorithm from subsection 7.1.1

   end

6. Apply one time step to the odd sites $|\Psi\rangle = U_o|\Psi\rangle$

7. Apply half a time step to the even sites $|\Psi\rangle = U_{he}|\psi_0\rangle$

8. Approximate the state with a state of lower bond dimension than D_{max} by using the algorithm from subsection 7.1.1

7.1.3 DMRG algorithm

The most efficient and accurate way to calculate the ground state of gapped Hamiltonians H for long spin chains is by DMRG. A corresponding algorithm may look like:

1. Write the Hamiltonian as a Matrix Product Operator $W_{[i]}$ (subsection 6.1.9)

2. Choose an initial state (either random or a guess of the ground state)

3. Prepare the initial state in canonical form with respect to the left site

4. Calculate all transfer matrices $R_{[i]}$ from $i = N$ to 1 and $L_{[1]}$. The transfer matrix $R_{[i]}$ is the contraction of all sites on the right of site i of the energy expectation value.

5. For $i = 1$ to N

   - Construct the effective Hamiltonian with respect to site i

   $$H_{eff}^{\alpha k \epsilon \gamma l \zeta} = L_{[i]}^{\alpha \beta \gamma} W_{[i]}^{\beta k l \delta} R_{[i]}^{\epsilon \delta \zeta}. \tag{7.5}$$

   This is the same as contracting all tensors of the expectation value of a Hamiltonian expect the ones at site i.

   - Reshape $H_{eff}^{\alpha k \epsilon \gamma l \zeta}$ to a $DdD \times DdD$ matrix

   - Calculate the lowest eigenvector $\tilde{A}$ of H_{eff}

   - Reshape $\tilde{A}$ to a $D \times d \times D$ tensor, and replace the old tensor with this new one $A_{[i]} = \tilde{A}$

   - Update the transfer matrix

   $$L_{[i+1]}^{\delta \epsilon \zeta} = L_{[i]}^{\alpha \beta \gamma} A_{[i]}^{\alpha k \delta} W_{[i]}^{\beta k l \epsilon} \bar{A}_{[i]}^{\gamma l \zeta} \tag{7.6}$$

   end

6. Do the same as in point 5 for $i = N : -1 : 1$ but update $R_{[i]}$ instead of $L_{[i]}$ after every time step

7. Calculate $\langle E \rangle$ of the new state and go to point 4 until $\langle E \rangle$ is converged

This algorithm can be improved by using a two-site algorithm and allows for the bond dimension between two sites to grow. This can be done equivalently as before but H_{eff} now reads in short hand notation $L_{[i]} W_{[i]} W_{[i+1]} R_{[i]}$ and moreover the loop goes from $i = 1$ until $i = N - 1$. In addition, the lowest eigenvector needs to be reshaped and decomposed into two tensors via a Schmidt decomposition where the unitary tensor replaces $A_{[i]}$ and the other one is inserted in canonical form into site $i + 1$.

8 Results and Discussion

8.1 Spin chain

We have investigated $\mathcal{PT}$-symmetric systems consisting of coupled harmonic oscillators with non-linear loss and gain both in the classical as well as in the quantum regime. We can now extend the analysis in the quantum regime by focusing on a typical quantum system, a spin chain Figure 2.2. We consider a spin chain of N cells each with two spins. The intracell coupling has strength g and the intercell h. The first spin in each cell is pumped with the rate Γ, and the second is damped with the same rate. Additionally, we include an overall damping rate κ. The Hamiltonian reads

$$\mathcal{H} = \frac{g}{2} \sum_{n=1}^{N/2} \left(\sigma_{2n-1}^+ \sigma_{2n}^- + \sigma_{2n-1}^- \sigma_{2n}^+ \right) + \frac{h}{2} \sum_{n=1}^{N/2-1} \left(\sigma_{2n}^+ \sigma_{2n+1}^- + \sigma_{2n}^- \sigma_{2n+1}^+ \right) \qquad (8.1)$$

and the master equation of this $\mathcal{PT}$-symmetric system is

$$\dot{\rho} = -\frac{i}{\hbar}[\mathcal{H}, \rho] + \frac{\Gamma}{2} \sum_{n=1}^{N/2} \mathcal{D}[\sigma_{2n-1}^+]\rho + \frac{\Gamma}{2} \sum_{n=1}^{N/2} \mathcal{D}[\sigma_{2n}^-]\rho + \kappa \sum_{n=1}^{N} \mathcal{D}[\sigma_n^-]\rho. \qquad (8.2)$$

In order to numerically solve this problem we vectorize this system:

$$\frac{d}{dt}|\rho\rangle = L|\rho\rangle. \qquad (8.3)$$

Instead of doing a time evolution until steady state is reached, we can directly calculate the steady state by finding the ground state of $L^\dagger L$ (see subsection 6.1.11). This is equivalent of finding the zero eigenvalue eigenstate of L, which equals the steady state solution of L. An advantage is that during the time evolution the state might only be represented with a high bond dimension although the bond dimension in the steady state is smaller.

Results of matrix product states calculations for a spin chain consisting of 10 spins with alternating gain and loss, equal coupling strength between the spin and an overall loss κ show that for low Γ/g the occupations of all spins coincide and the
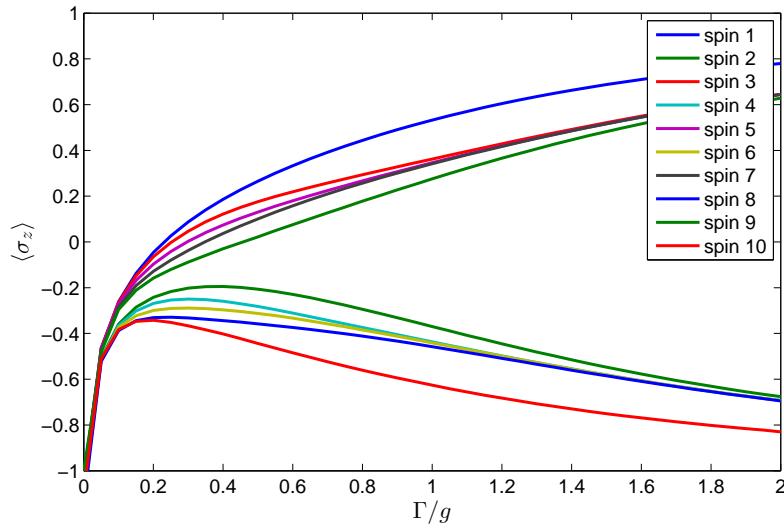
Figure 8.1: Results of matrix product states calculations for a spin chain consisting of 10 spins with alternating gain and loss Γ and a coupling strength $g = h$ and an overall loss $\kappa = 0.05g$. For low Γ/g, the occupations of all spins coincide, while for higher Γ/g the occupation alternates between high and low between the different sites.

system is $\mathcal{PT}$-symmetric while for higher Γ/g the occupation alternates between high and low population and the $\mathcal{PT}$-symmetry is broken. One can clearly see that every second spin is similarly populated in the broken regime except the spins on the edge. From this fact and simulations with longer spin chains (not shown here) we can conclude that we can expect only minor differences for longer spin chains.

9 Conclusion

In this work, we investigated $\mathcal{PT}$-symmetry breaking in the quantum regime. In the first part we focused on the steady state properties of a system consisting two coupled oscillators where one experiences non-linear gain and the other one non-linear loss. We focused on an implementation by coupled conventional optical lasers and by coupled phonon lasers with NV-centers in diamond. In the case of conventional optical lasers, simulations with quantum trajectories as well as stochastic differential equations showed that for high Γ/g the occupation differs but no phase transition occurs and the $\mathcal{PT}$-symmetry is only weakly broken. The result holds true in the classical regime as well as in the quantum regime.

However, simulations for the two coupled phonon lasers revealed that $\mathcal{PT}$-symmetry breaking exists not only in the classical case, but also in the quantum regime in the presence of intrinsic quantum noise. Moreover, simulations showed that the $\mathcal{PT}$-symmetric region is very noisy and the amplitudes are governed by the overall loss κ, while in the $\mathcal{PT}$-broken region there are low fluctuations and the system can be described by two coherent states. Furthermore, the mean occupations coincide with the purely classical solutions in the broken regime. A dramatic drop of fluctuations at the phase transition not only occurs for the mean occupation, moreover it can be observed for the current between the two system.

We demonstrated that the symmetry breaking point moves to higher Γ/g the more quantum a system is. Moreover, we could explain this phenomenon by noise activation. Furthermore, quantum trajectory simulations showed that a higher level of quantum noise leads to a broadening of the transition over a wider range of Γ/g.

We extended our analysis not only to the quantum regime, moreover we additionally studied typical quantum systems as coupled two-level systems such as spin chains. Matrix Product State simulations verified that $\mathcal{PT}$-symmetry breaking also exists in spin chains.

From our results we can conclude that $\mathcal{PT}$-symmetry breaking is exists not only in classical systems but can also be observed in the quantum regime as well as in typical quantum systems.

Bibliography

[1] Carl M Bender and Stefan Boettcher. Real spectra in non-hermitian hamiltonians having p t symmetry. *Physical Review Letters*, 80(24):5243, 1998.

[2] Carl M Bender. Making sense of non-hermitian hamiltonians. *Reports on Progress in Physics*, 70(6):947, 2007.

[3] Hui Jing, SK Özdemir, Xin-You Lü, Jing Zhang, Lan Yang, and Franco Nori. Pt-symmetric phonon laser. *Physical review letters*, 113(5):053604, 2014.

[4] Xun-Wei Xu, Yu-xi Liu, Chang-Pu Sun, and Yong Li. Mechanical pt symmetry in coupled optomechanical systems. *Physical Review A*, 92(1):013852, 2015.

[5] Xin-You Lü, Hui Jing, Jin-Yong Ma, and Ying Wu. P t-symmetry-breaking chaos in optomechanics. *Physical review letters*, 114(25):253601, 2015.

[6] Christian E Rüter, Konstantinos G Makris, Ramy El-Ganainy, Demetrios N Christodoulides, Mordechai Segev, and Detlef Kip. Observation of parity–time symmetry in optics. *Nature Physics*, 6(3):192–195, 2010.

[7] Joseph Schindler, Ang Li, Mei C Zheng, Fred M Ellis, and Tsampikos Kottos. Experimental study of active lrc circuits with pt symmetries. *Physical Review A*, 84(4):040101, 2011.

[8] Carl M Bender, Bjorn K Berntson, David Parker, and E Samuel. Observation of pt phase transition in a simple mechanical system. *arXiv preprint arXiv:1206.4972*, 2012.

[9] K.V. Kepesidis, T.J. Milburn, K. G. Makris, S. Rotter, and P. Rabl. Pt-symmetry breaking phenomena in the steady state of coupled phonon lasers. *arXiv:1508.00594*, 2015.

[10] Hamidreza Ramezani, Tsampikos Kottos, Ramy El-Ganainy, and Demetrios N Christodoulides. Unidirectional nonlinear pt-symmetric optical structures. *Physical Review A*, 82(4):043803, 2010.

[11] Daniel F Walls and Gerard J Milburn. *Quantum optics*. Springer Science & Business Media, 2007.

[12] KV Kepesidis, SD Bennett, S Portolan, Mikhail D Lukin, and P Rabl. Phonon cooling and lasing with nitrogen-vacancy centers in diamond. *Physical Review B*, 88(6):064105, 2013.

[13] Goran Lindblad. On the generators of quantum dynamical semigroups. *Communications in Mathematical Physics*, 48(2):119–130, 1976.

[14] Roy J Glauber. Coherent and incoherent states of the radiation field. *Physical Review*, 131(6):2766, 1963.

[15] ECG Sudarshan. Equivalence of semiclassical and quantum mechanical descriptions of statistical light beams. *Physical Review Letters*, 10(7):277, 1963.

[16] Hannes Risken. *Fokker-planck equation*. Springer, 1984.

[17] Crispin Gardiner. *Stochastic methods*. Springer Berlin, 2009.

[18] Klaus Mølmer, Yvan Castin, and Jean Dalibard. Monte carlo wave-function method in quantum optics. *J. Opt. Soc. Am. B*, 10(3):524–538, Mar 1993.

[19] Desmond J Higham. An algorithmic introduction to numerical simulation of stochastic differential equations. *SIAM review*, 43(3):525–546, 2001.

[20] Wikipedia. Linear dynamical system, 2016. [Online; accessed 23-June-2016].

[21] Guifré Vidal. Efficient simulation of one-dimensional quantum many-body systems. *Physical review letters*, 93(4):040502, 2004.

[22] Frank Verstraete, Valentin Murg, and J Ignacio Cirac. Matrix product states, projected entangled pair states, and variational renormalization group methods for quantum spin systems. *Advances in Physics*, 57(2):143–224, 2008.

[23] Ulrich Schollwöck. The density-matrix renormalization group in the age of matrix product states. *Annals of Physics*, 326(1):96–192, 2011.

[24] Guifre Vidal, José Ignacio Latorre, Enrique Rico, and Alexei Kitaev. Entanglement in quantum critical phenomena. *Physical review letters*, 90(22):227902, 2003.

[25] Gene H Golub and Christian Reinsch. Singular value decomposition and least squares solutions. *Numerische mathematik*, 14(5):403–420, 1970.

[26] David Perez-Garcia, Frank Verstraete, Michael M Wolf, and J Ignacio Cirac. Matrix product state representations. *arXiv preprint quant-ph/0608197*, 2006.

[27] Juan José García-Ripoll. Time evolution of matrix product states. *New Journal of Physics*, 8(12):305, 2006.

[28] Eduardo Mascarenhas, Hugo Flayac, and Vincenzo Savona. Matrix-product-operator approach to the nonequilibrium steady state of driven-dissipative quantum arrays. *Physical Review A*, 92(2):022116, 2015.

[29] Jian Cui, J Ignacio Cirac, and Mari Carmen Bañuls. Variational matrix product operators for the steady state of dissipative quantum systems. *Physical review letters*, 114(22):220601, 2015.

[30] Guifre Vidal. Classical simulation of infinite-size quantum lattice systems in one spatial dimension. *Physical review letters*, 98(7):070201, 2007.

[31] David Perez-Garcia, Frank Verstraete, J Ignacio Cirac, and Michael M Wolf. Peps as unique ground states of local hamiltonians. *arXiv preprint arXiv:0707.2260*, 2007.